ChemSusChem

Review
doi.org/10.1002/cssc.202301926

Chemistry Europe
European Chemical Societies Publishing

www.chemsuschem.org

Optimized Transition Metal Phosphides for Direct Seawater Electrolysis: Current Trends

Yong Li,*[a] Tianran Xin,[a] Zongcheng Cao,[a] Weiran Zheng,[b] Peng He,*[a] and Lawrence Yoon Suk Lee*[c]

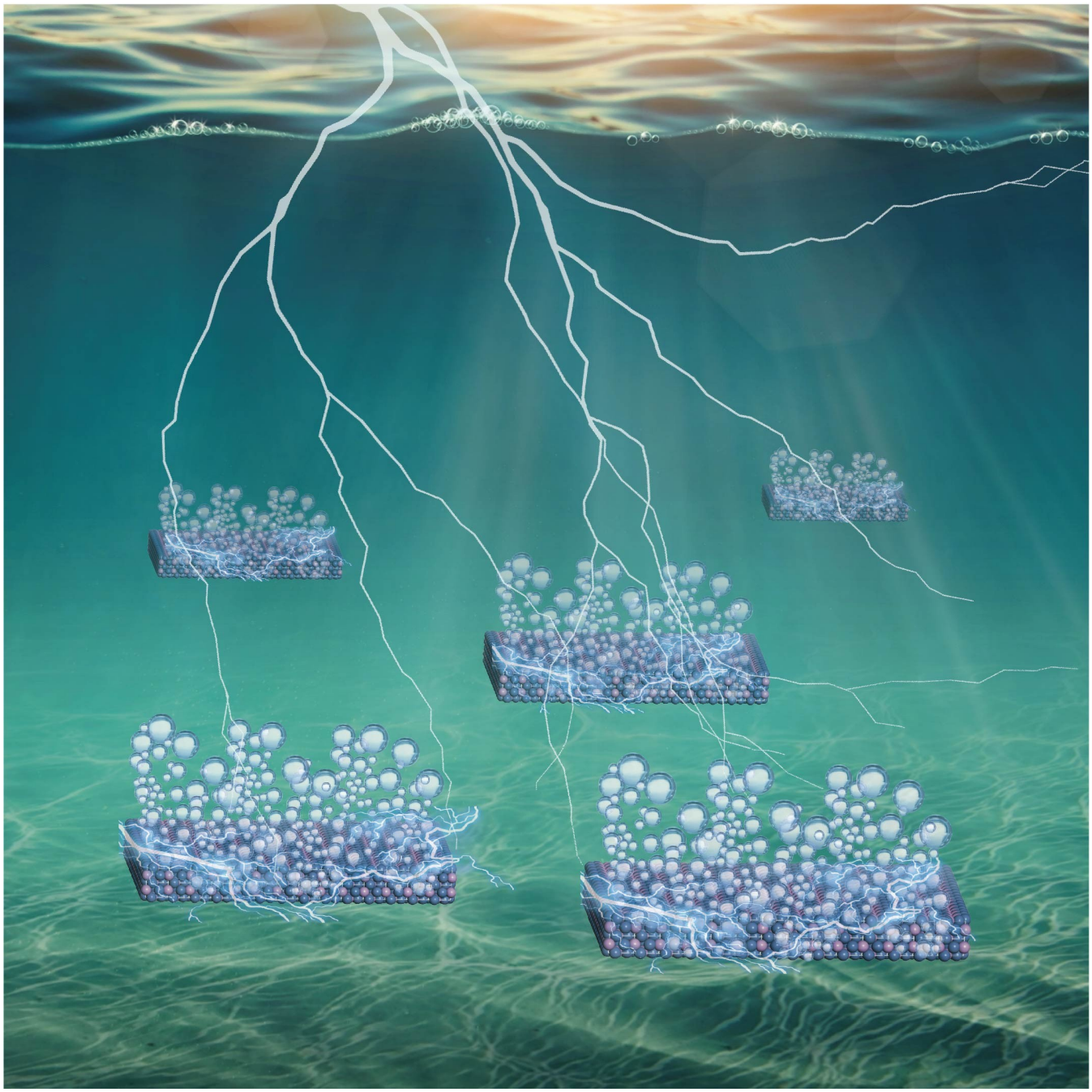

Seawater electrolysis presents a viable route for sustainable large-scale hydrogen production, yet its practical application is hindered by several technical challenges. These include the sluggish kinetics of hydrogen evolution, poor stability, cation deposition at the cathode, electrode corrosion, and competing chloride oxidation at the anode. To overcome these obstacles, the development of innovative electrocatalysts is crucial. Transition metal phosphides (TMPs) have emerged as promising candidates owing to their superior catalytic performance and tunable structural properties. This review provides a comprehensive analysis of recent progress in the structural engineering of TMPs tailored for efficient seawater electrolysis. We delve into the catalytic mechanisms underpinning hydrogen and oxygen evolution reactions in different pH conditions, along with the detrimental side reactions that impede hydrogen production efficiency. Several methods to prepare TMPs are then introduced. Additionally, detailed discussions on structural modifications and interface engineering tactics are presented, showcasing strategies to enhance the activity and durability of TMP electrocatalysts. By analyzing current research findings, our review aims to inform ongoing research endeavors and foster advancements in seawater electrolysis for practical and ecologically sound hydrogen generation.

1. Introduction

Fossil fuels such as oil, coal, and natural gas currently remain the primary sources of global energy demand.[1] However, the anticipated depletion of these finite sources and their greenhouse gas emissions have led to critical climate changes and a looming energy crisis worldwide. It is urgent and of paramount importance to search for clean and renewable energy sources for sustainable development. Hydrogen has been considered a promising next-generation energy carrier with its high energy density.[2] The majority (~96%) of industrial hydrogen is now being produced through steam reforming and coal gasification, but these processes involve the formation of CO_2 and require high energy input. Electrocatalytic water splitting is widely recognized as a promising, clean, cost-effective hydrogen production solution, garnering extensive research attention.[3] Alkaline water electrolyzers (AWEs) and proton exchange membrane electrolyzers (PEMEs) represent the mainstream of current commercial water splitting technologies, which necessitate high-purity water for hydrogen generation. Typically, high-purity water is sourced from freshwater supplies, favored for their low levels of contaminants and the relative ease of purification. However, as we pivot towards a hydrogen-based energy infrastructure, the demand for massive volumes of freshwater could exacerbate existing global water scarcity concerns. This raises critical questions about the sustainability of such technologies in the context of the planet's limited freshwater resources. Driess *et al.* argued that even if all of the global energy consumption for one year were used to generate hydrogen through water splitting, the freshwater consumption would only represent 0.4% of global freshwater usage.[4] However, these figures are based on current energy consumption rates, ignoring regional disparities.

On the other hand, Li and co-workers suggested that if the average energy consumption per person worldwide matched that of the United States, the freshwater consumption for hydrogen production could rise to 8–10%.[5] In light of technological progress and societal growth, a surge in energy consumption is anticipated, intensifying the pressure on already strained freshwater resources for hydrogen fuel production. This impending scenario underscores the urgency of identifying and harnessing alternative water sources for hydrogen generation.

Seawater, which makes up 97% of our planet's water, offers a vast resource for hydrogen production and could ease the strain on our limited freshwater. But seawater's complexity, brimming with organisms and various impurities, poses a challenge. To harness it for energy, we must cleverly navigate these hurdles, ensuring we can tap into this abundant source without compromise. The most significant difference between freshwater and seawater is the salt content, with seawater containing approximately 3.5 wt.% of salt per unit, equivalent to *ca.* 0.5 M NaCl electrolyte containing other ions such as Mg^{2+}, Ca^{2+}, and K^{+}. One advantage of seawater is its high conductivity (up to 5 S m^{-1}), which is significantly higher than freshwater (5.5×10^{-6} S m^{-1}).[6] However, there are also drawbacks. The primary challenge is the chloride oxidation reaction (COR), which generates toxic, environmentally harmful, and corrosive Cl_2 or ClO^{-}. While Cl_2 and ClO^{-} have industrial applications such as sterilization, water purification, and chemical manufacturing,[7] their demands are much lower than those for hydrogen. To prevent undesired COR, a certain amount of base (KOH or NaOH) is dissolved into seawater to adjust the pH to above 7.5. This maximizes the difference in thermodynamic overpotentials between the oxygen evolution reaction (OER) and COR, reducing the likelihood of COR. Developing effective

[a] *Dr. Y. Li, T. Xin, Z. Cao, Dr. P. He*
School of Materials Science and Engineering
Anhui Polytechnic University
Wuhu 241000, Anhui, China
E-mail: yong.li@mail.ahpu.edu.cn
hepeng@ahpu.edu.cn

[b] *Prof. W. Zheng*
Department of Chemistry and Guangdong Provincial Key Laboratory of Materials and Technologies for Energy Conversion
Guangdong Technion-Israel Institute of Technology
Shantou 515063, China

[c] *Prof. L. Yoon Suk Lee*
Department of Applied Biology and Chemical Technology and Research Institute for Smart Energy
The Hong Kong Polytechnic University
Hung Hom, Kowloon, Hong Kong SAR, China
E-mail: lawrence.ys.lee@polyu.edu.hk

electrocatalysts is crucial to enhance the selectivity of OER over COR at the anode and improve the hydrogen evolution reaction (HER) activity at the cathode. In traditional water splitting, noble metal-based catalysts, such as Pt-based catalysts for HER and RuO_2/IrO_2 for OER, are considered the most promising electrocatalysts. However, these catalysts face challenges when applied to seawater splitting. Pt-based electrocatalysts, for example, are susceptible to poisoning by Cl^- ions due to the strong formation of Pt—Cl bonds.[8] Therefore, Pt-based electrocatalysts are unsuitable for direct seawater splitting. Additionally, the high cost and limited availability of noble metal-based electrocatalysts greatly restrict their widespread use.[9]

Transition metal-based electrocatalysts have emerged as a promising alternative for HER and OER due to their adjustable properties and affordability. This diverse group encompasses materials such as oxides, hydroxides, sulfides, nitrides, selenides, and carbides of transition metals, which have shown good potentials in efficiently catalyzing water splitting reaction.[10] Among these materials, transition metal phosphides (TMPs) have shown great promise for HER and OER in both acidic and alkaline media, demonstrating high intrinsic activity and tunable structure.[11] TMPs have been extensively studied to understand their catalytic mechanisms. Firstly, the unique electronic structure of phosphorus in TMPs enables it to readily capture electrons from adjacent metal atoms, weakening the M–H bond strength and facilitating hydrogen desorption.[12] Secondly, P atoms can act as proton acceptors, allowing the adsorption of H^+ ions and promoting H—OH bond breaking.[13] Thirdly, TMPs undergo significant surface reconstruction under OER conditions, forming numerous active sites for oxygen production and release.[14] Fourthly, TMPs exhibit the remarkable capability to be easily tailored onto various surfaces, including transition metals, oxides, borides, carbides, and chalcogenides. This versatility results in potent synergistic

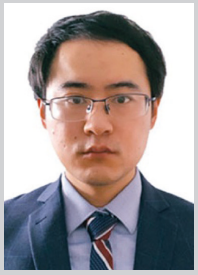

Dr. Yong Li is currently a lecturer of School of Materials Science and Engineering in Anhui Polytechnic University. He obtained his Ph.D. at Department of Applied Biology and Chemical Technology in The Hong Kong Polytechnic University in 2021. His current research is focused on functional nanomaterials synthesis and electrocatalysis.

Tianran Xin is an undergraduate student at School of Materials Science and Engineering in Anhui Polytechnic University under the supervision of Dr. Yong Li. Her research focuses on the synthesis of novel nanostructured materials and the water splitting performance evaluation.

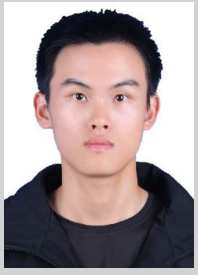

Zongcheng Cao is an undergraduate student at School of Materials Science and Engineering in Anhui Polytechnic University under the supervision of Dr. Yong Li. His research focuses on the electrooxidation of organic compounds coupled with hydrogen evolution.

Dr. Peng He obtained his doctoral degree in materials science and engineering from Beijing Institute of Technology (2017–2021). He is currently a lecturer of School of Materials Science and Engineering in Anhui Polytechnic University. His research focuses on the low dimensional electromagnetic functional materials.

Prof. Weiran Zheng is an associate professor of chemistry at the Guangdong Technion-Israel Institute of Technology (GTIIT). He was a Research Fellow at The Hong Kong Polytechnic University after obtaining his Ph.D. degree from Wuhan University, China. His research focuses on understanding the activation and deactivation mechanisms of electrocatalysts from an atomic scale. He specializes in operando techniques coupled with electrocatalytic processes, such as spectroelectrochemistry and atomic force microscopy.

Prof. Lawrence Yoon Suk Lee received his Ph.D. degree from McGill University, Canada. He is currently an associate professor at the Hong Kong Polytechnic University, Hong Kong SAR. Engaging state-of-the-art characterization techniques, such as in situ Raman, operando TEM, and in situ XRD, his research group focuses on understanding the atomic structure of nanomaterials for various electorcatalytic processes, including water splitting and CO_2 reduction, as well as lithium-sulfur and sodium-ion batteries.

effects that significantly enhance water splitting.[15] Lastly, through surface engineering techniques, the electronic and crystal structures of TMPs can be readily modified to further enhance their electrocatalytic activity toward water splitting.[16] The exceptional physicochemical and electrocatalytic properties of TMPs make them highly suitable for direct seawater splitting. Further interfacial modifications allow for tailoring and optimizing the electrocatalytic performance of TMPs, making them well-suited for efficient and sustainable hydrogen production from seawater.

This review presents a detailed examination of how the structural engineering of TMPs influences their electrocatalytic efficacy in direct seawater splitting. We illustrate the latest surface modification strategies that enhance TMPs' seawater splitting performance, as shown in Scheme 1. We first assess the fundamental mechanisms of HER and OER within both acidic and alkaline environments, and then address the challenges presented by potential side reactions in seawater splitting, such as chloride oxidation, which can impede the process's efficiency and selectivity. Following this, we introduce several common methods to prepare TMPs and explore a range of structural modification techniques that have been applied to improve TMPs' intrinsic activity for seawater splitting, including the use of amorphous polymetallic phosphides, doping with metals and non-metals, co-doping techniques, heterostructure modifications, and integrated approaches combining these methods. The discussion proceeds to interface engineering strategies that mitigate side reactions in seawater splitting. These include manipulating the TMP surface with surface reconstruction, oxyhydroxide modification, modification with negatively charged compounds, carbon layer coverage, and creating 3D hierarchical structures. The review culminates by offering insights into designing highly efficient electrocatalysts tailored for direct seawater splitting, intending to guide future advancements in this area.

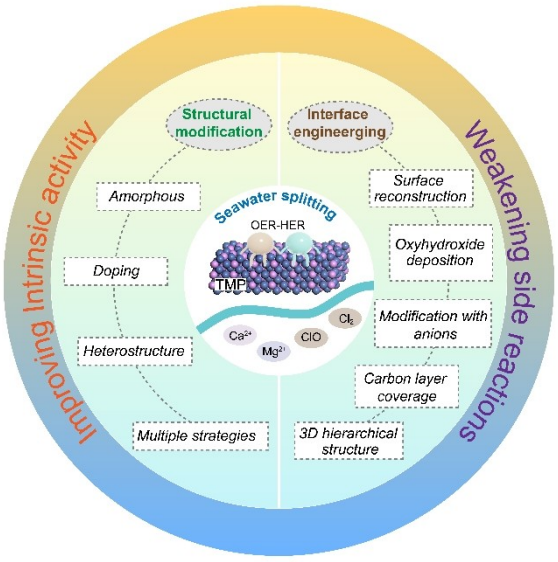

Scheme 1. Strategies to improve the intrinsic activity of TMPs toward seawater splitting and suppress side reactions.

2. Mechanism of Water Splitting

2.1. Water Splitting in Acidic and Alkaline Media

Water splitting consists of two half-reactions: OER at the anode and HER at the cathode. The pathways for these reactions differ in acidic or alkaline electrolytes:

Acidic conditions:

$$\text{Anode}: \ 2H_2O \rightarrow O_2 + 4H^+ + 4e^- \quad (1)$$

$$\text{Cathode}: \ 4H^+ + 4e^- \rightarrow 2H_2 \quad (2)$$

Alkaline conditions:

$$\text{Anode}: \ 4OH^- \rightarrow O_2 + 2H_2O + 4e^- \quad (3)$$

$$\text{Cathode}: \ 2H_2O + 2e^- \rightarrow H_2 + 2OH^- \quad (4)$$

Water splitting demands a thermodynamic potential of 1.23 V (*vs.* standard hydrogen electrode, SHE) as the HER is favored under acidic conditions and the OER is more efficient under alkaline conditions.[5,17]

2.2. Seawater Splitting

Compared to water splitting in high-purity acidic or alkaline solutions, the direct usage of seawater presents additional challenges due to its complex composition.[4] Table 1 demonstrates that Na^+ and Cl^- species account for approximately 86 wt.% of the impurities in seawater. Na^+ ions are commonly considered safe and advantageous in water splitting due to their ability to enhance the electrolyte's conductivity without actively participating in the electrochemical reactions. However,

Table 1. Typical concentration of components present in seawater at 20 °C.[4]

Species	Concentration (ppm)
Cl^-	19,400
Na^+	10,800
SO_4^{2-}	2,700
Mg^{2+}	1,300
Ca^{2+}	400
K^+	400
HCO_3^-	100
Br^-	70
$B(OH)_3$	30
CO_3^{2-}	10
Sr^{2+}	10
F^-	1
Other inorganic elements	0.6
Organic matters	1–2
Dissolved gases (N_2, O_2, Ar)	19

high Na^+ concentration in seawater can still affect electrode fouling and corrosion.

The presence of Cl^- ions is more problematic for seawater electrolysis as it can be oxidized to ClO^- or Cl_2, (reactions 5 and 6), which are toxic, environmentally harmful, and corrosive.

$$\textit{Chlorine evolution}: \ 2Cl^- \rightarrow Cl_2 + 2e^- \quad (5)$$

$$\textit{ClO}^- \textit{ generation}: \ 2Cl^- + 2OH^- \rightarrow ClO^- + 4H_2O + 2e^- \quad (6)$$

While ClO^- and Cl_2 can have beneficial applications, such as in disinfection or chemical synthesis, the demand for these chemicals is generally lower than for hydrogen in water splitting processes. Collecting and utilizing ClO^- and Cl_2 can also be challenging and complex. Furthermore, seawater typically has a pH of 8.0 to 8.3, meaning neither H^+ nor OH^- ion concentrations are high. In neutral pH, the adsorption and dissociation of water molecules are considered the rate-determining step for forming H^+ and OH^- in seawater splitting. This step introduces a significant energy barrier and slows down the overall kinetics of the water-splitting process. To overcome these challenges in seawater splitting, enhancing the selectivity and activity of anodic electrocatalysts is crucial to promote the OER and avoid undesired COR.

The Pourbaix diagram for an aqueous saline electrolyte, as depicted in Figure 1, demonstrates that the pH of the electrolyte has a considerable impact on the products of the COR.[18] In an acidic environment ($pH < 3$), chlorine gas (Cl_2) readily forms, while hypochlorite ions (ClO^-) become increasingly favored across a wide pH range from 3 to 14. As the pH shifts from alkaline (14) towards acidic (1), the thermodynamic potential for COR deviates from linearity, signifying that the kinetics of COR are faster in acidic and neutral conditions than in alkaline ones. Nonetheless, OER consistently exhibits a lower energy barrier than COR throughout the pH spectrum, suggesting that OER will be the preferred reaction. Notably, in an alkaline solution, there is a persistent potential difference of about 480 mV between the standard potentials of OER and COR, which is more substantial than the difference in acidic or neutral conditions. Consequently, utilizing alkaline seawater can be strategically advantageous to reduce the occurrence of COR during direct seawater splitting processes.[19]

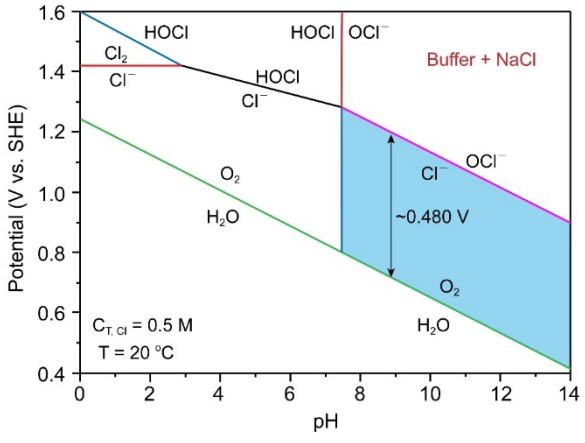

Figure 1. Pourbaix diagram of an aqueous saline electrolyte. Reproduced with permission from Ref. [18]. Copyright 2016, Wiley-VCH.

Alongside the challenges associated with COR, the presence of Ca^{2+} and Mg^{2+} ions in seawater is also problematic. Due to the low solubility (K_{sp}) of $Ca(OH)_2$ and $Mg(OH)_2$ (4×10^{-4} and 5.61×10^{-12}, respectively), these insoluble hydroxides are easily formed under alkaline conditions and can deposit on the surface of electrodes, particularly the cathode. Such deposits impede the charge transfer rate and block the active sites, diminishing the overall efficiency of the water-splitting process.[20] An entirely effective method to address this complication has not been identified. The most prevalent strategy to date involves designing electrocatalysts with expansive surface areas, which helps alleviate the impact of hydroxide deposition by providing more active sites for the reaction to occur.

3. Synthetic Methods of TMPs

TMPs, denoted as M_xP_y, are composed of metal and phosphorus. The $3s^23p^3$ electronic configuration in the third shell of phosphorus affords five vacant 3D orbitals that can draw electrons from metal atoms to form M–P bonds.[21] Therefore, M and P in M_xP_y carry partial positive and negative charges, respectively. The electropositive M atoms in TMPs exhibit a weakened ability to adsorb H*, which is critical for HER activity, facilitating H_2 generation.[22] On the other hand, the electronegative P atoms can also act as active sites to capture H* to improve the HER performance through an ensemble effect between the adjacent transition metal and phosphorus atoms. When TMPs serve as anodic catalysts, the surface of TMPs is easily converted to metal hydroxide/oxyhydroxide which is regarded as the real active species for OER.[23] The *in situ*-generated heterostructures show an increased OER activity. Furthermore, the electronic and crystal structures of TMPs can be readily modified to further enhance their electrocatalytic activity. It is worth noting that the synthesis of phase-pure TMPs remains challenging due to their diverse compositions, encompassing M_3P, M_5P_2, $M_{12}P_5$, M_2P, M_5P_4, MP, MP_2, and MP_3. The distinct crystal structures formed during different steps of synthesis alter the coordinate environments of M and P, thereby influencing their electrocatalytic activity. Consequently, the rational design of TMP structures, considering these factors, unveils their superior intrinsic activity, offering new avenues for exploring seawater splitting possibilities. To date, several synthetic methods have been reported to prepare TMPs with a variety of nanostructures.

3.1. Hydrothermal/Solvothermal Method

The one-step hydrothermal synthesis is commonly used to create nanostructured TMPs and offers a large flexibility in tuning the composition by adjusting the reaction conditions.[24] In this case, a growth solution is prepared by mixing the

transition metal salt and phosphorus source in an aqueous solution and then transferred into an autoclave reactor to react at a mild temperature and high pressure. The phosphorus source encompasses red phosphorus, white phosphorus, and sodium hypophosphite (NaH_2PO_2). The structure of M_xP_y can be precisely adjusted by controlling the molar ratio of transition metal ions and phosphorus in the growth solution. The roles of solvent, temperature, and heating time are critical in determining the phase and morphology of TMPs. When the aqueous solution is replaced by organic solvents, such as oleylamine, 1-octadecene, and toluene, the growth of TMPs is controlled by a solvothermal process, which takes place in an inert gas-filled three-neck flask.[25] Owing to the high boiling points (~350 °C) of these organic solvents, the reaction temperature can go up to 200~300 °C and generate TMPs at atmospheric pressure. In this case, organic phosphines, such as triphenyl phosphate and trioctylphosphine are employed as the phosphorus sources.

Typically, the hydrothermal or solvothermal method is not used alone. These methods are employed to synthesize precursors which need to follow another post-phosphorization treatment to form TMPs. Different from the one-step generation, the morphology of the precursor can be well preserved after the post-phosphorization treatment, yielding the expected structure of TMPs. For example, metal-organic frameworks (MOFs) are promising precursors for synthesizing TMPs.[26] MOFs are assembled by the interconnection of inorganic nodes with organic ligands, which is usually accomplished by a hydrothermal/solvothermal approach. Thanks to the unique porous structure of MOFs, the TMPs prepared using MOFs exhibit high porosity and large specific surface area, which is preferable for use in electrocatalysis.

3.2. Solid-Gas Reaction

A solid-gas reaction occurs when a substance is treated with phosphorus gas, resulting in the formation of TMPs, which is fast and convenient. One common approach involves annealing the target in a tubular furnace. Red phosphorus was the first reported as the source to form phosphorus vapor in an inert atmosphere at a certain temperature (~500 °C) and react with the substance.[27] Thereafter, NaH_2PO_2 has been employed as the P source, which can decompose to release PH_3 at only 300 °C. The PH_3 then reacts with the substance through an anion exchange strategy to form TMPs.[28] Due to the lower annealing temperature required when using NaH_2PO_2 compared to red phosphorus, it is widely adopted to synthesize TMPs. However, the rapid decomposition rate of NaH_2PO_2 poses a challenge, as the formed PH_3 may not fully react with the precursor. As a consequence, the mass of NaH_2PO_2 employed is typically higher than the theoretical mass necessary to synthesize the target phase. Plasma treatment is another way to realize the solid-gas reaction to prepare TMPs. When the precursor is placed in the chamber of a plasma-enhanced chemical vapor deposition system that is filled with PH_3 atmosphere, the substance can be efficiently converted to TMPs under plasma treatment at a low temperature.[29]

In comparison with the hydrothermal/solvothermal method, the TMPs prepared by solid-gas reactions show a higher purity and typically exhibit better electrocatalytic activity. However, the molar ratio of metal and phosphorus in M_xP_y is difficult to control by this method. Moreover, the released toxic PH_3 gas makes this synthesis process very dangerous and inhibits large-scale preparation and application. Hence, developing a straightforward and eco-friendly method is imperative in the preparation of TMPs.

3.3. Electrodeposition

Electrodeposition is a viable alternative method for the production of TMPs, offering advantages in terms of cost-effectiveness, simplicity in setup, and scalability.[30] Typically employed within a standard three-electrode system, electrodeposition comprises a working electrode, a counter electrode, and a reference electrode. Diverse TMP composite structures can be achieved by selecting various types of working electrodes, including flat plates, porous foams, and 3D substrates. The manipulation of deposition parameters, such as voltage, current, and bath composition, further allows for the attainment of a broad spectrum of nanostructured TMP morphologies. The direct deposition of material onto the electrode surface ensures robust adhesion, minimizing potential loss during subsequent use. Significantly, electrodeposition is commonly carried out at room temperature, leading to the formation of amorphous phases in the deposited TMPs.[31] While amorphous TMPs may lack the structural stability seen in those synthesized through hydrothermal or solid-gas methods, they offer distinct advantages, such as a large specific surface area and abundant exposed active sites. Consequently, achieving optimal catalytic response and stability for amorphous structured TMPs hinges on precise control of the electrodeposition process.

4. Recent Developments of TMPs in Seawater Splitting

TMPs have shown great potential as effective catalysts for both HER and OER in a wide range of pH values. These materials possess several advantages such as good electrical conductivity, thermal stability, high electrocatalytic activity, and the ability to adjust their crystal structure, making them highly attractive for various applications. Recently, the use of TMPs for seawater splitting has gained significant attention, and it has demonstrated exceptional performance as highlighted in Table 2. To further improve the performance of TMPs in seawater splitting, two methods have been explored: structural modification to enhance intrinsic activity and interface engineering to mitigate side reactions. These approaches aim to meet higher standards regarding superior intrinsic activity, precise selective oxidation, and improved corrosion resistance.

Table 2. Summary of recently reported TMP-based electrocatalysts for seawater splitting.

Catalyst	Electrolyte	Electrolyzer	Cell voltage at 100 mA cm^{-2}	Stability
Co–Fe_2P[33]	1 M KOH + 0.5 M NaCl	Co–$Fe_2P_{(+)}$||Co–$Fe_2P_{(-)}$	1.69 V	22 h
Mo–CoP_x/NF[34]	1 M KOH + seawater	Mo–CoP_x/$NF_{(+)}$||Mo–CoP_x/$NF_{(-)}$	2.16 V	100 h
Cr–Co_xP[35]	1 M KOH + seawater	Cr–$Co_xP_{(+)}$||Cr–$Co_xP_{(-)}$	1.85 V	160 h
N–$NiMo_3P$[36]	1 M KOH + seawater	N–$NiMo_3P_{(+)}$||N–$NiMo_3P_{(-)}$	1.55 V at 10 mA cm^{-2}	24 h
B,V–Ni_2P[37]	1 M KOH + 0.5 M NaCl	$NiFeOOH_{(+)}$||B,V–$Ni_2P_{(-)}$	1.64 V	–
Ru/B–CoP[38]	1 M KOH + seawater	$NiFe_{(+)}$||Ru/B–$CoP_{(-)}$	1.64 V at 10 mA cm^{-2}	11 h
Ni_2P–Fe_2P/NF[39]	1 M KOH + seawater	Ni_2P–Fe_2P/$NF_{(+)}$||Ni_2P–Fe_2P/$NF_{(-)}$	1.811 V	48 h
Ni_2P–FeP/FF[40]	1 M KOH + 0.5 M NaCl	NiFe–LDH/$FF_{(+)}$||Ni_2P–FeP/$FF_{(-)}$	1.53 V at 10 mA cm^{-2}	20 h
NiPS/NF[41]	1 M KOH + seawater	NiPS/$NF_{(+)}$||NiPS/$NF_{(-)}$	1.68 V	60 h
Mn–Ni_2P/Fe_2P[42]	1 M KOH + seawater	Mn–Ni_2P/$Fe_2P_{(+)}$||Mn–Ni_2P/$Fe_2P_{(-)}$	2.02 V	120 h
RuV–CoNiP/NF[43]	1 M KOH + seawater	RuV–CoNiP/$NF_{(+)}$||RuV–CoNiP/$NF_{(-)}$	1.809 V	24 h
FCNP@CQDs/CP[44]	1 M KOH + seawater	FCNP@CQDs/$CP_{(+)}$||FCNP@CQDs/$CP_{(-)}$	1.61 V	50 h
CoP_x@FeOOH[45]	1 M KOH + seawater	CoP_x@$FeOOH_{(+)}$||$CoP_{x(-)}$	1.710 V	80 h
Co_xP_v@NC[46]	6 M KOH + seawater	Co_xP_v@$NC_{(+)}$||Co_xP_v@$NC_{(-)}$	1.74 V at 1,000 mA cm^{-2}	100 h
C@CoP–FeP/FF[47]	1 M KOH + 0.5 M NaCl	C@CoP–FeP/$FF_{(+)}$||C@CoP–FeP/$FF_{(-)}$	1.73 V	100 h
Ni@Ni_2P@NiCoP[48]	1 M KOH + 0.5 M NaCl	Ni@Ni_2P@NiCoP$_{(+)}$||Ni@Ni_2P@NiCoP$_{(-)}$	1.822 V at 300 mA cm^{-2}	24 h
$Ru_{22}NiMoP_2$[49]	1 M KOH + seawater	$Ru_{22}NiMoP_{2(+)}$||$Ru_{22}NiMoP_{2(-)}$	1.53 V at 10 mA cm^{-2}	20 h
NiP_x@HA[50]	1 M KOH + 0.5 M NaCl	NiP_x@$HA_{(+)}$||NiP_x@$HA_{(-)}$	1.63 V	40 days
Fe_2P/$Ni_{1.5}Co_{1.5}N$/Ni_2P[51]	1 M KOH + seawater	Fe_2P/$Ni_{1.5}Co_{1.5}N$/$Ni_2P_{(+)}$||Fe_2P/$Ni_{1.5}Co_{1.5}N$/$Ni_2P_{(-)}$	1.624 V	40 h
$(Fe_{0.74}Co_{0.26})_2P$/Ni_3N[52]	1 M KOH + seawater	Fe_2P/$Ni_3N_{(+)}$||$(Fe_{0.74}Co_{0.26})_2P$/$Ni_3N_{(-)}$	1.64 V	70 h

4.1. Improvement of Intrinsic Activities by Structural Modification

As previously discussed, adjusting the pH of seawater to a high value of 8–14 by adding NaOH or KOH significantly increases the standard potential difference between the OER and COR, which ultimately enhances the selectivity of OER over COR. Additionally, improving the intrinsic OER and HER activities of TMPs, with overpotentials under 200 mV at 10 mA cm^{-2}, can also help prevent the occurrence of COR.[32] Such boost of intrinsic activity is commonly assisted by structural modification, such as adjusting crystallinity, doping, and introducing heterogeneous structures.

4.1.1. Amorphous Polymetallic Phosphides

Polymetallic phosphides present several benefits when compared to their monometallic counterparts, particularly in electrocatalysis. A primary advantage is their superior electrical conductivity, attributed to the synergistic effect of incorporating various metallic elements. This enhanced conductivity is crucial for facilitating electron transfer during electrocatalytic reactions. Additionally, the amalgamation of different metals within polymetallic phosphides provides the flexibility to engineer the electronic properties at the active sites. Fine-tuning these electronic states optimizes the adsorption and desorption energies of reaction intermediates such as adsorbed oxygen species (O*) and hydrogen species (H*). This fine-tuning is pivotal for improving the efficiency and selectivity of electrocatalytic processes, including those involved in energy conversion and storage applications.[53] Additionally, the design of amorphous polymetallic phosphides has gained attention for its potential to enhance intrinsic activity. Amorphous structures lack long-range order and possess a high degree of structural disorder. This structural characteristic results in a large number of catalytically active sites and their accessibility. The efficient structure transformation in amorphous polymetallic phosphides can further optimize the catalytic performance by creating new active sites or exposing different surface facets. For instance, Li's group prepared two kinds of amorphous NiFeP structures, namely nanosheet (NS) and nanowire (NW, Figure 2a), for HER and OER in simulated alkaline seawater (1.0 M KOH + 0.01 M $KHCO_3$ + 1 M NaCl).[54] After undergoing an electrochemical activation, both amorphous NiFeP NS and NW demonstrated improved catalytic performance compared to their initial states. The NiFeP NW required overpotentials of 100 and 129 mV in OER to reach the current densities of 10 and 100 mA cm^{-2}, respectively (Figure 2b). The enhanced OER activity was attributed to the formation of an amorphous metal oxyhydroxide species and the presence of P after the activation process, as confirmed by *in situ* Raman spectroscopy (Figure 2c). Density functional theory (DFT) calculations indicated that incorporating P atoms into NiFeOOH could significantly lower the energy barrier for converting HO* to HOO* species, promoting efficient oxygen evolution. Interestingly, the activation process only slightly changed the surface structure of amorphous NiFeP NS. However, the HER activity of NiFeP NS was significantly

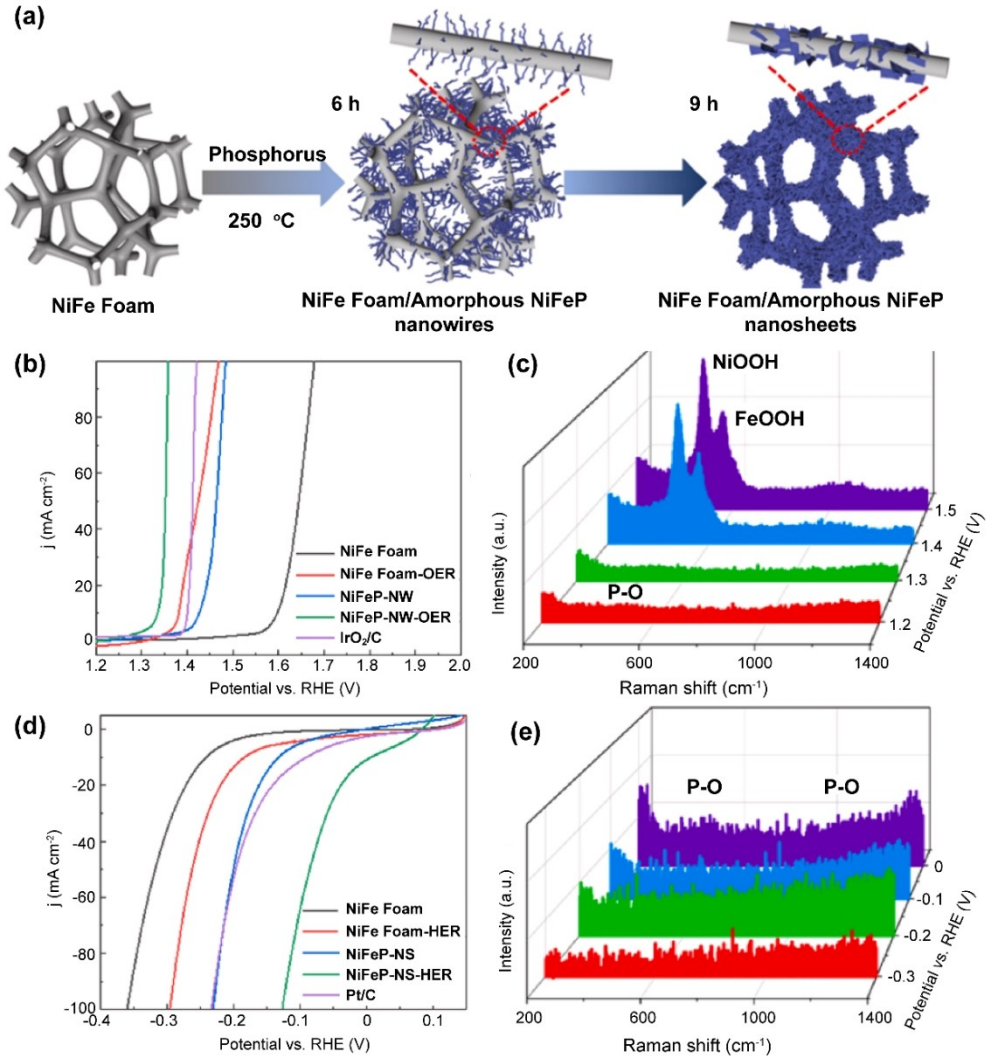

Figure 2. (a) Schematics showing the synthetic procedure of amorphous NiFeP NW and NS on NiFe foam. (b) Anodic polarization plots of NiFe foam, NiFe foam-OER, NiFeP-NW, NiFeP-NW-OER, and IrO_2/C. (c) *In situ* Raman spectra of NiFeP-NW. (d) Cathodic polarization plots of NiFe foam, NiFe foam-HER, NiFeP-NS, NiFeP-NS-HER, and Pt/C. (e) *In situ* Raman spectra of NiFeP-NS. Reproduced with permission from Ref. [54]. Copyright 2022, Elsevier.

improved, surpassing that of commercial Pt/C (Figure 2d). X-ray photoelectron spectroscopy (XPS) and *in situ* Raman spectroscopy revealed notable changes in the P $2p_{3/2}$ peak position and the peak intensities of P–O vibrations at 473 and 551 cm^{-1}, respectively (Figure 2e). These changes indicated the degradation of surface phosphate species, which optimized the hydrogen adsorption and desorption energies during the HER process.

4.1.2. Metal Doping

Metal doping has proven to be an efficacious strategy for modulating the electronic state of phosphides. This process involves the integration of heteroatoms that either substitute for atoms in the original lattice or become intercalated within the lattice interstices. Such alterations in the phosphide structure can significantly influence its electronic and catalytic properties.

In a study by Lin *et al.*, the CoP with various crystal phases and morphologies were successfully synthesized by manipulating the amount of Fe doping. This variation in Fe content allowed for quantitatively examining how metal doping affects the electrocatalytic behavior of phosphides. The Fe dopants could potentially modify the electronic density and structural arrangement of CoP, thereby enhancing its performance in catalytic applications.[55] When the Co-to-Fe molar ratio changed from 1:0 to 1:1.2, the nanoparticle morphology was changed to nanorods with the crystal structure transition from CoP to Co_2P.

At a Co-to-Fe ratio of 1:0.5, single-phased Co_2P with well-defined nanorod bundles was formed, exhibiting the best HER activity with the smallest overpotential compared to other samples. In 0.5 M H_2SO_4, 1 M KOH, and neutral seawater, the overpotentials required to reach 10 mA cm^{-2} were 159, 156, and 489 mV, respectively. The enhanced HER activity of the Fe-

doped Co_2P was attributed to the downshifting of the *d*-band center which weakened the hydrogen binding strength. The Gibbs free energy of hydrogen adsorption (ΔG_{H^*}) for Fe-doped Co_2P was measured to be 0.67 eV, lower than that of Co_2P (0.9 eV) and Mn-doped Co_2P (0.71 eV).

In another study by Ma and colleagues, a 3D heterostructure of Co-doped Fe_2P was prepared for the catalysis of seawater splitting.[33] Bader charge transfer calculations confirmed that Co dopants acted as active sites by contributing partial electrons to the adsorbed hydrogen, optimizing the Gibbs free energy of H_2 generation. Co–Fe_2P exhibited better performance of overall seawater splitting with a required voltage of 1.69 V at 100 mA cm^{-2} compared to the commercial RuO_2||Pt–C (1.97 V). Sun and co-workers studied the overall seawater splitting activity of Co-doped Ni_2P (Co–Ni_2P).[56] According to the DFT calculations, the value of ΔG_{H^*} for Co–Ni2P (0.52 eV) was slightly larger than that of pristine Ni_2P (0.45 eV). However, the energy barrier for water dissociation on Co–Ni_2P (0.69 eV) was much lower than that of Ni_2P (1.03 eV), indicating the superior HER activity of Co–Ni_2P in alkaline electrolytes. Adding dimethyl sulfoxide (DMSO) in the growth solution was critical in generating a unique bristlegrass-like morphology for Co–Ni_2P, which provided abundant active sites for alkaline seawater splitting. When engaged as a bifunctional electrocatalyst, the Co–Ni_2P||Co–Ni_2P system delivered a voltage of 1.71 V at 50 mA cm^{-2}, lower than RuO_2||Pt–C (1.91 V). Tian's group introduced Mo dopants into CoP nanosheets grown on Ni foam (Mo–CoP_x/NF).[34] The unique Mo–P–Co bonds in the Mo–CoP_x/NF||Mo–CoP_x/NF electrolyzer resulted in better overall seawater splitting performance than RuO_2||Pt–C. Song and co-workers synthesized vein-like Cr-doped Co_xP (Cr–Co_xP) as a bifunctional electrocatalyst for overall seawater splitting.[35] The structure of Cr–CoxP was proved by X-ray diffraction (XRD) pattern and scanning electron microscopic (SEM) image (Figures 3a and b). The work function of Cr–Co_xP decreased from 4.84 to 3.74 eV, indicating higher electronic conductivity (Figure 3c). In an electrolyte containing 1 M KOH and 0.5 M NaCl, the OER and HER overpotentials required to achieve 1,000 mA cm^{-2} were 423 and 282 mV, respectively, which was comparable to those in 1 M KOH (Figures 3d and e). However, the catalytic activities slightly decreased in seawater containing 1 M KOH due to impurities. The excellent catalytic activity of Cr–Co_xP was attributed to the Cr^{6+} dopants that had a strong proton capture property, enhancing the seawater splitting activity of Co atoms. Cr–Co_xP also exhibited higher corrosion potential and lower corrosion current density than Co_xP (Figure 3f), revealing excellent anti-corrosion capability after Cr doping. DFT calculations confirmed

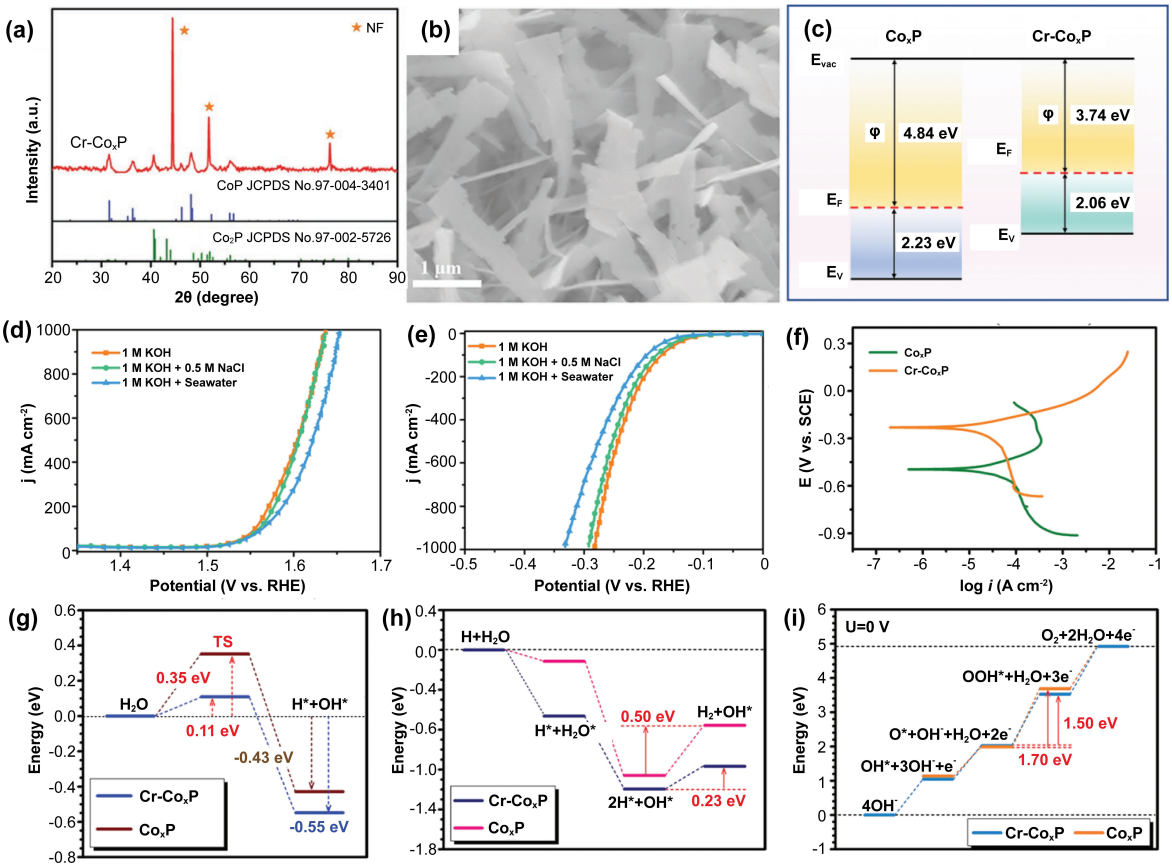

Figure 3. (a) XRD and (b) SEM image of Cr–Co_xP. (c) Work functions of Co_xP and Cr–Co_xP. (d) Anodic and (e) cathodic polarization plots of Cr–Co_xP in 1 M KOH, 1 M KOH + 0.5 M NaCl, and 1 M KOH + seawater. (f) Corrosion polarization curves of Co_xP and Cr–Co_xP in natural seawater. DFT calculations on the reaction energies of Cr–Co_xP and Co_xP for (g) water dissociation, (h) HER under alkaline solution, and (i) OER under U = 0 V. Reproduced with permission from Ref. [35]. Copyright 2023, Wiley-VCH.

that the energy barriers for water dissociation, hydrogen evolution, and oxygen evolution in Cr–Co_xP were lower than those of pristine Co_xP (Figures 3g to i), validating the improved water-splitting activity of Cr–Co_xP.

4.1.3. Non-Metal Doping

Non-metal dopants, which often possess a stronger electronegativity and a smaller atomic radius than phosphorus, can also be instrumental in tailoring the electronic properties of TMPs. When these non-metal atoms substitute for phosphorus within the TMP lattice, they can induce changes in the electronic structure due to their different atomic characteristics.

Cheng and co-workers synthesized carbon-doped Co_2P for HER in an alkaline seawater electrolyte containing mixed chlorides (NaCl, $MgCl_2$, and $CaCl_2$, Figure 4a).[57] C–Co_2P exhibited an HER overpotential of only 30 mV at 10 mA cm^{-2}, surpassing the activity of commercial Pt/C catalyst (34 mV). The C–Co_2P also showed good stability at current densities of 10, 100, and 1,000 mA cm^{-2} for 20 h, outperforming Pt/C (Figure 4c). The incorporation of carbon in Co_2P shifted the *d*-band center from −1.567 to −1.615 eV (Figure 4d), resulting in weaker Co−H* bonds compared to pristine Co_2P. DFT calculations confirmed the elongated Co−H* bond length in C–Co_2P (Figure 4e). Furthermore, due to the stronger electronegativity and smaller atomic radius of C compared to P, C atoms acted as electron acceptors, facilitating H* adsorption and water dissociation for enhanced H_2 formation rate (Figure 4f). Loomba *et al.* introduced N atoms into $NiMo_3P$ to form stable metal-N (M–N) bonds, resulting in N-doped $NiMo_3P$ (N–$NiMo_3P$).[36] N–$NiMo_3P$, with abundant M–N bonds, demonstrated remarkable performance in seawater splitting. The HER overpotential was only 35 mV at 10 mA cm^{-2} and the overall seawater splitting voltage to achieve 10 mA cm^{-2} was 1.55 V. The outstanding performance of N–$NiMo_3P$ was attributed to the generated M–N bonds, which improved the stability of the active site and decreased the diffusion of impurities to the surface of N–$NiMo_3P$.

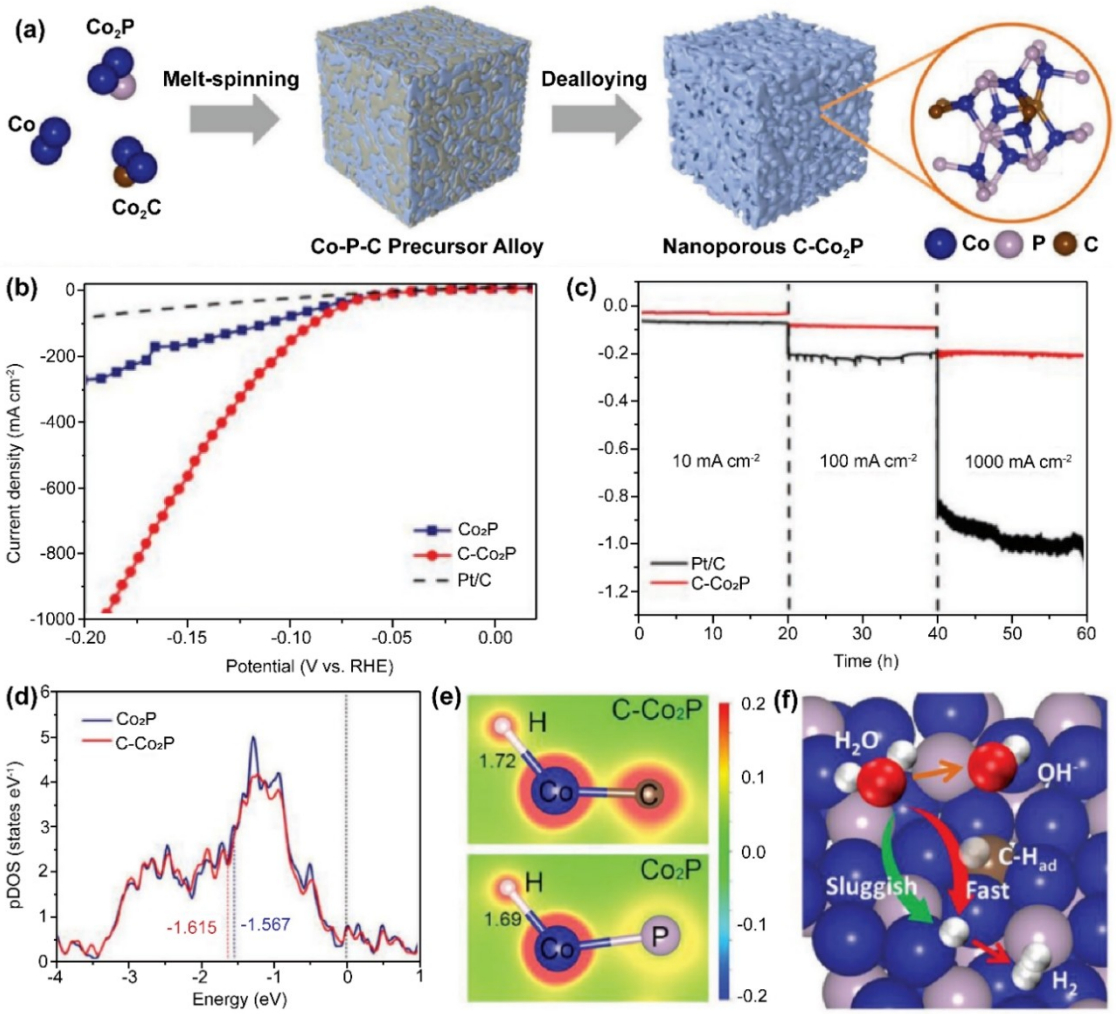

Figure 4. (a) Schematic synthetic procedure for nanoporous C–Co_2P. (b) Polarization curves of Co_2P, C–Co_2P, and Pt/C. (c) Galvanostatic curves of C–Co_2P in simulated alkaline seawater at 10, 100, and 1,000 mA cm^{-2} for 20 h. (d) pDOS of Co 3*d* orbital and (e) charge density distribution of Co atoms in Co_2P and C–Co_2P. (f) Illustration of HER on C–Co_2P. Reproduced with permission from Ref. [57]. Copyright 2023, Wiley-VCH.

4.1.4. Metal–Non-Metal Co-Doping

The co-doping strategy, which involves the simultaneous incorporation of metal and non-metal elements into a host material, has indeed been explored to synergize the benefits of different dopants in enhancing the properties of TMPs. Metal dopants typically modify the local electronic structure and crystallographic properties of the host material. They can also introduce new active sites or improve the electrical conductivity, facilitating the charge transfer necessary for electrocatalysis.

Non-metal dopants, on the other hand, are often more electronegative than phosphorus. They can affect the electronic properties by creating more localized states, modifying the band structure, or increasing the binding strength of reactants and intermediates.

Zhao's group prepared B and V co-doped Ni_2P (B,V–Ni_2P), which exhibited favorable properties for the HER in simulated seawater.[37] Compared to individually doped B–Ni_2P and V–Ni_2P, B,V–Ni_2P demonstrated the lowest water dissociation energy, Gibbs free energy of hydrogen adsorption, and a significantly downshifted *d*-band center. B,V–Ni_2P achieved an HER overpotential of 74 mV at 10 mA cm^{-2}, outperforming V–Ni_2P and pristine Ni_2P, and exhibited excellent electrocatalytic stability in simulated seawater. A two-electrode seawater electrolyzer was constructed using B,V–Ni_2P as the cathode and NiFeOOH as the anode, which achieved a cell voltage of 1.64 V at 100 mA cm^{-2}, surpassing the performance of the commercial IrO2||Pt/C system. The NiFeOOH||B,V–Ni_2P configuration was also employed in an anion exchange membrane water electrolyzer (AEMWE) and demonstrated a low cell voltage of 1.78 V at 500 mA cm^{-2}. Wang *et al.* developed Ru and B co-doped CoP (Ru/B–CoP) for HER in a wide pH range, including seawater.[38] The Ru/B co-doping significantly enhanced the HER activity of CoP in various electrolytes, such as 0.5 M H_2SO_4, 1 M phosphate-buffered solution (PBS), 1 M KOH, and seawater containing 1 M KOH, compared to Ru–CoP, B–CoP, and CoP catalysts. An electrolytic cell device with a NiFe||Ru/B–CoP configuration achieved a voltage of 1.64 V to reach 10 mA cm^{-2} in 1 M KOH + seawater, which was lower than the NiFe||NiFe system. Additionally, the same group synthesized Fe and F co-doped Ni_2P (Fe,F–Ni_2P) for hydrogen production in seawater.[58] However, due to the instability of Fe,F–Ni_2P under high potentials caused by surface oxidation, hydrazine oxidation reaction (HzOR) was employed as a replacement for the oxygen evolution reaction (OER) on Fe,F–Ni_2P. The Fe,F–Ni_2P catalyst was used as both the anode and cathode in seawater containing 1 M KOH and 0.5 M N_2H_4, requiring only 0.57 V to achieve 1 A cm^{-2}.

4.1.5. Heterostructure Modification

Combining phosphides with other materials such as sulfides, nitrides, and oxides in seawater-splitting catalysts can create synergistic effects that enhance performance. This strategy leverages the complementary properties of each material to improve electrical conductivity, stability against corrosion, and the kinetics of electrochemical reactions. The result is a catalyst with more active sites, optimized adsorption and desorption of reaction intermediates, and improved structural characteristics, such as increased surface area and porosity. These enhancements can lead to reduced overpotentials and higher efficiency in the electrolysis process.

Zheng's group employed a hydrothermal method and phosphorization to synthesize a heterostructure of Ni_2P/Ni_5P_4.[59] The Ni_2P/Ni_5P_4 interface exhibited an energy barrier for water dissociation of only 0.28 eV, which is lower than that of Ni_2P (0.69 eV) and Ni_5P_4 (0.37 eV, Figures 5a and b). The Gibbs free energy of hydrogen generation at the Ni_2P/Ni_5P_4 interface was −0.113 eV, closer to zero than pristine Ni_2P (−0.398 eV) and Ni_5P_4 (−0.202 eV, Figures 5c and d)), indicating superior HER activity. The Ni_2P/Ni_5P_4 catalyst demonstrated a slightly increased overpotential in 1 M KOH + seawater compared to 1 M KOH or 1 M KOH + 0.5 M NaCl (Figure 5e). A NiFe–LDH||Ni_2P/Ni_5P_4 electrolyzer exhibited similar performance in seawater, 1 M KOH, and 1 M KOH + 0.5 M NaCl (Figure 5f). Wu *et al.* reported self-supported Ni_2P–Fe_2P nanosheets grown on a Ni foam (Ni_2P–Fe_2P/NF), which showed improved HER activity compared to Ni_2P–Ni_5P_4/NF and $Ni(OH)_2$/NF catalysts in 1 M KOH (Figures 5g and h).[39] The OER and HER overpotentials of Ni_2P–Fe_2P/NF were 218 and 128 mV at 10 mA cm^{-2}, respectively. The Ni_2P–Fe_2P/NF electrolyzer demonstrated excellent overall water splitting activity in 1 M KOH with a cell voltage of 1.682 V to reach 100 mA cm^{-2}, outperforming the Pt/C||IrO_2 system. When applied in 1 M KOH + seawater, the required voltage increased to 1.811 V to drive 100 mA cm^{-2}, with a smaller voltage difference compared to the Pt/C||IrO_2 system, indicating better anti-interference capability in a seawater environment. Li and co-workers prepared a similar catalyst, Ni_2P–FeP on a Fe foam (Ni_2P–FeP/FF), using an oxygen corrosion method followed by phosphorization.[40] The HER overpotentials of Ni_2P–FeP/FF were only 42 and 89 mV at 10 mA cm^{-2} in 1 M KOH and saline water (1 M KOH + 0.5 M NaCl), respectively. The assembled NiFe–LDH||Ni_2P–FeP/FF electrolyzer required a voltage of 1.53 V at 10 mA cm^{-2}. Pan's group synthesized a multi-phase heterostructure of CoNiP/Co_xP (x = 1 and 2) to enhance HER activity in seawater splitting.[60] The overpotential of CoNiP/Co_xP was only 36 mV at 10 mA cm^{-2} in 1 M KOH, which was significantly lower than other catalysts such as CoP/NiCoP/NC,[61] Ni/NiCoP,[62] and NiCoP–CoP/NF.[63] In natural seawater, CoNiP/Co_xP also exhibited superior HER activity with a small onset overpotential of 82 mV and an overpotential of 290 mV at 10 mA cm^{-2}, outperforming pristine Ni_xP and Co_xP. DFT calculations revealed that the superior intrinsic activity of CoNiP/Co_xP resulted from the presence of CoNiP/Co_2P and CoNiP/CoP interfaces, which optimized the Gibbs free energy of hydrogen generation (Figure 5j) and facilitated water dissociation (Figure 5k), respectively. The HER process of CoNiP/Co_xP followed the Volmer–Heyrovsky reactions at the interface of CoNiP and CoP (Figure 5l). Other heterostructures have also been recently reported, which include Cu_3P–FeP,[64] sandwich-like NiCoN/Ni_xP/NiCoN,[15a] Ni_2P/NiS_2,[41] FeMnS/FeMnP/NF,[15b] and $CeO_2/Co_{0.4}Ni_{1.6}P$.[15c]

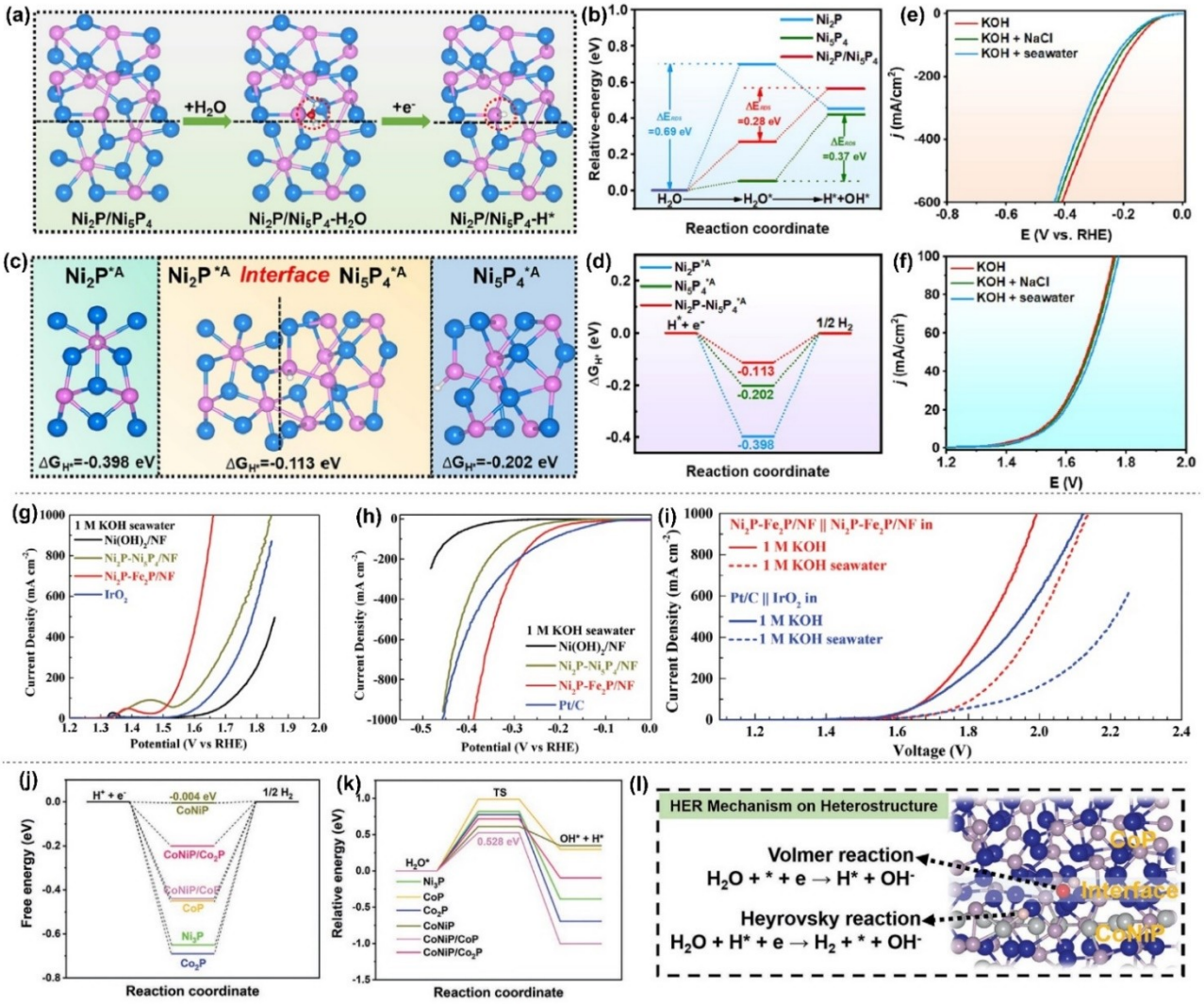

Figure 5. (a) HER mechanism of Ni_2P/Ni_5P_4 in alkaline media. (b) Energy barriers of water dissociation, (c) Gibbs free energy of H* adsorption, and (d) DFT calculations of H_2 generation on Ni_2P, Ni_5P_4, and Ni_2P/Ni_5P_4. (e) Cathodic and (f) anodic polarization plots of Ni_2P/Ni_5P_4 in 1 M KOH, 1 M KOH + 0.5 M NaCl, and 1 M KOH + seawater. Reproduced with permission from Ref. [59]. Copyright 2023, Elsevier. (g) Anodic and (h) cathodic polarization plots of $(NiOH)_2$/NF, Ni_2P–Ni_5P_4/NF, Ni_2P–Fe_2P/NF, and Pt/C in 1 M KOH + seawater. (i) Overall water/seawater splitting activities of Ni_2P–Fe_2P/NF and Pt/C||IrO_2 in 1 M KOH and 1 M KOH + seawater. Reproduced with permission from Ref.39. Copyright 2020, Wiley-VCH. DFT calculations of (j) H_2 generation and (k) water dissociation on Ni_3P, CoP, Co_2P, CoNiP, CoNiP/CoP, and CoNiP/Co_2P. (l) Illustration of HER on NiCoP/Co_xP. Reproduced with permission from Ref. [60]. Copyright 2021, Wiley-VCH.

4.1.6. Multiple Strategies

Recent research in seawater splitting has focused on combining multiple modification strategies to design highly active TMP-based electrocatalysts. One such example is the work by Shi's group, who synthesized Mn-doped Ni_2P/Fe_2P catalysts for effective seawater splitting.[42] The Mn-doped Ni_2P/Fe_2P catalyst exhibited lower overpotentials for both HER and OER compared to Ni_2P/Fe_2P, Mn-doped Ni_2P, and Mn-doped Fe_2P. In alkaline seawater, the overpotentials for Mn-doped Ni_2P/Fe_2P were measured as 358 mV for HER and 470 mV for OER to reach 1 A cm^{-2}. The catalyst also showed excellent stability, maintaining a stable current density even at 500 mA cm^{-2} for over 200 h. The cell voltage of a Mn-doped Ni_2P/Fe_2P||Mn-doped Ni_2P/Fe_2P electrolyzer for overall seawater splitting was estimated to be 2.02 V at 500 mA cm^{-2}. *Ex situ* XPS analysis confirmed that the improved seawater splitting performance was due to the formation of Mo-doped NiFe oxides/oxyhydroxides during the OER process and Mn-doped Ni–Fe hydroxides during the HER process.

Ruthenium has also been investigated as an incorporation element in TMPs due to its similar M–H* bonding strength to Pt. Incorporating Ru can optimize the adsorption energies of intermediates involved in the OER and HER on P sites.[65] Additionally, Ru incorporation can induce electronic redistribution and modify electrical conductivity.[66] Mu *et al.* introduced Fe dopants to regulate the amorphous-crystal structure of NiP_2 nanosheets grown on Ni foam and prepared Ru nanocrystals anchored on Ni(Fe)P_2 (Ru–Ni(Fe)P_2/NF) for seawater splitting.[67] The Ru–Ni(Fe)P_2/NF catalyst exhibited low overpotentials of

520 mV for OER and 361 mV for HER at 1 A cm^{-2} in alkaline seawater. The catalyst showed high electronic conductivity, as indicated by charge density difference calculations, which showed a high accumulation of electrons at the Ru–Ni(Fe)P_2/NF interface. The Gibbs free energy of hydrogen generation on Ru–Ni(Fe)P_2/NF was closer to zero than that of Ru–NiP_2/NF, confirming the superior HER activity of Ru–Ni(Fe)P_2/NF. DFT calculations estimated the energy barrier for the OER process, showing that Ru–Ni(Fe)P_2/NF had a lower barrier (0.86 eV) compared to Ru–NiOOH/NF (1.10 eV), which indicated better OER activity for Ru–Ni(Fe)OOH/NF. In a study conducted by Ma and colleagues, a Ru,V co-doped CoP/Ni_2P (RuV–CoNiP) heterostructure was synthesized as a bifunctional electrocatalyst for HER and OER in seawater splitting.[43] Compared to Ru-doped CoP/Ni_2P (Ru–CoNiP) and V-doped CoP/Ni_2P (V–CoNiP), RuV–CoNiP exhibited higher electrical conductivity and more exposed active sites, leading to enhanced activity for seawater splitting. The RuV–CoNiP||RuV–CoNiP electrolyzer demonstrated low voltage requirements, with 1.538, 1.663, and 1.809 V needed to reach 20, 50, and 100 mA cm^{-2}, respectively. In another study, Wang's group employed a microwave method to grow Ru nanoclusters on the surface of hollow-structured B-doped FeP (Ru/h–B–FeP) for HER in alkaline seawater.[68] The interaction between Ru and B–FeP resulted in an overpotential of only 99 mV to reach 10 mA cm^{-2}, which was lower than Ru,B co-doped FeP (122 mV) and FeP (262 mV).

4.2. Prevention of Side Reactions by Interface Engineering

Seawater electrolysis faces challenges from high concentrations of salts such as NaCl, $CaCl_2$, and $MgCl_2$, which can cause competitive reactions and chloride corrosion. A promising solution to protect anodic electrocatalysts during the OER is creating a protective polyanionic layer on their surface to repel Cl^- ions. Researchers have developed various innovative methods to induce a negatively charged coating on TMPs, including surface reconstruction, oxyhydroxide modification, application of negatively charged compounds, and carbon layer deposition. Additionally, the adoption of 3D hierarchical structures in electrocatalysts has effectively prevented the accumulation of $Mg(OH)_2$ and $Ca(OH)_2$ on the electrode surface. These structures enhance the surface area and improve the diffusion of reactants and products, thereby minimizing the risks of deposition-related degradation and enhancing corrosion resistance.

4.2.1. Surface Reconstruction

Surface reconstruction refers to the *in situ* generation of a polyanion layer on the surface of TMPs-based electrocatalysts due to the operation in high potential ranges. The $M^{2/3+}$ and $P^{1/2-}$ ions are easily oxidized to $M(OH)_x$, MOOH, and PO_4^{3-}, respectively. Huang *et al.* synthesized a bimetal (Co and Fe) modified Ni_2P on Ni foam, demonstrating efficient and durable electrocatalytic activity for seawater splitting.[69] The CoFe-co-doped Ni_2P (CoFe–Ni_2P) exhibited superior performance for the OER and HER compared to Co–Ni_2P, Fe–Ni_2P, and pristine Ni_2P. CoFe–Ni_2P required OER overpotentials of only 266 and 304 mV at large current densities of 100 and 500 mA cm^{-2}, respectively, in seawater containing 6 M KOH (Figure 6a). Moreover, even after operating at 500 mA cm^{-2} for 600 h, the overpotential of CoFe–Ni_2P increased by only 70 mV, indicating its excellent stability (Figure 6b). *In situ* Raman spectroscopy revealed the formation of NiOOH during the OER process (Figure 6c), and Co–Ni_2P generated Co–NiOOH species at a lower potential compared to Fe–Ni_2P (Figures 6d and e). The CoFe–Ni_2P also exhibited a similar trend of structural evolution (Figure 6f), suggesting that Co dopants played a more significant role than Fe dopants in accelerating the transformation of NiOOH, thereby providing abundant active sites for OER. The corrosion resistance of CoFe–Ni_2P was found to be superior to Co–Ni_2P, Fe–Ni_2P, and pristine Ni_2P, with the lowest corrosion current density (18.58 μA cm^{-2}) and the highest corrosion potential (−0.492 V *vs.* Hg/HgO, Figure 6g). DFT calculations indicated that CoFe–NiOOH had the highest selectivity for adsorbing OH^- ions over Cl^- ions, as evidenced by the largest Gibbs adsorption free energy difference between Cl^- and OH^- ($\Delta G_{*Cl-*OH}$ = 3.48 eV) compared to NiOOH (0.33 eV), Co–NiOOH (0.87 eV), and Fe–NiOOH (1.20 eV, Figure 6h). These results demonstrated the superior OER selectivity of CoFe–Ni_2P over COR. CoFe–Ni_2P was also active for HER (Figure 6i) and exhibited 210 and 270 mV overpotentials at 100 and 500 mA cm^{-2}, respectively, in seawater containing 6 M KOH. Furthermore, when used in an electrolyzer configuration, the CoFe–Ni_2P electrolyzer achieved a low voltage of 1.690 V to reach a current density of 100 mA cm^{-2} in 1 M KOH (Figure 6j). The voltage slightly increased to 1.725 V in 1 M KOH + seawater and 1.738 V in 6 M KOH + seawater conditions. Additionally, CoFe–Ni_2P was grown on Ni-felt and applied in an AEM electrolyzer configuration (Figure 6k). In this setup, the CoFe–Ni_2P-based AEM electrolyzer exhibited a low cell voltage of 2.25 V at 1.0 A cm^{-2}.

Wang's group designed a carbon-quantum-dots-embedded Fe/Co/Ni phosphide (FCNP@CQDs) electrocatalyst, which also exhibited strong surface reconstruction for seawater splitting.[44] The OER performance of FCNP@CQDs was superior to other electrocatalysts such as FCNP, FCN LDH@CQDs, and FCN-LDHs. FCNP@CQDs demonstrated an OER overpotential of only 268 mV at 20 mA cm^{-2} in alkaline seawater, which was much lower than FCNP (281 mV), FCN LDH@CQDs (288 mV), andFCN-LDHs (311 mV). Furthermore, the FCN-LDHs exhibited good HER performance with a low overpotential of 150 mV at 20 mA cm^{-2}, which was also superior to FCNP, FCN LDH@CQDs, and FCN-LDHs. XPS results of FCNP@CQDs before and after OER revealed significant changes. Peaks corresponding to Fe−P, Co−P, and P–M disappeared, and new peaks with high binding energy were formed after OER. These changes indicated the formation of PO_x-modified Fe/Co/Ni oxide/oxyhydroxides, which were responsible for the improved OER activity and electrostatic repulsion of Cl^- ions.

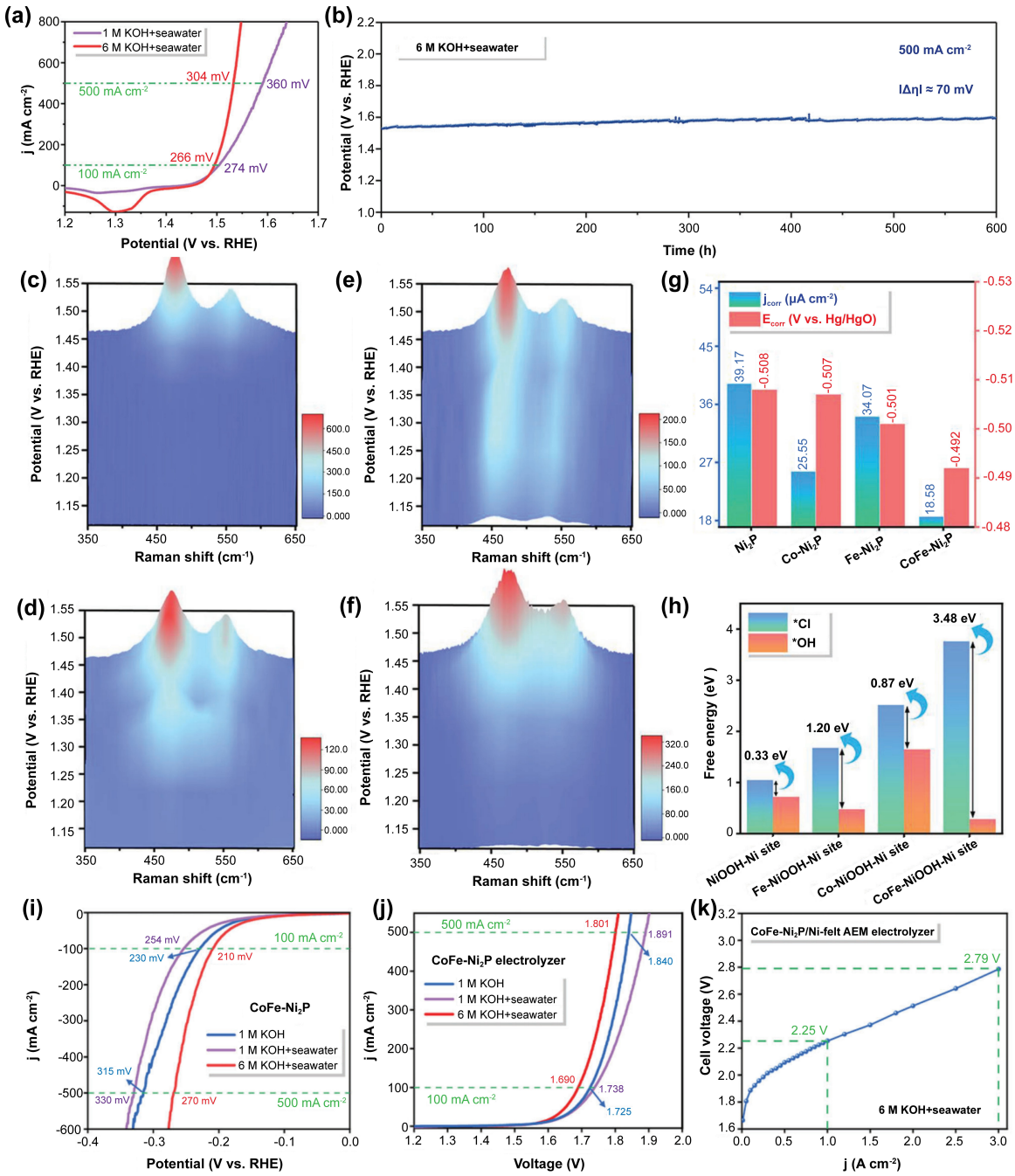

Figure 6. (a) Anodic polarization plots of CoFe–Ni_2P in 1 M KOH + seawater and 6 M KOH + seawater. (b) Chronopotentiogram of CoFe–Ni_2P at 500 mA cm^{-2} in 6 M KOH + seawater for 600 h. *In situ* Raman spectra of (c) Ni_2P, (d) Fe–Ni_2P, (e) Co–Ni_2P, and (f) CoFe–Ni_2P. (g) Corrosion potential and corrosion current density of Ni_2P, Fe–Ni_2P, Co–Ni_2P, and CoFe–Ni_2P. (h) Adsorption energies of *Cl and *OH at the Ni sites of NiOOH, Fe–NiOOH, Co–NiOOH, and CoFe–NiOOH. (i) Cathodic polarization curves of CoFe–Ni_2P and (j) polarization curves of CoFe–Ni_2P electrolyzer in 1 M KOH, 1 M KOH + seawater, and 6 M KOH + seawater. (k) Catalytic activity of CoFe–Ni_2P/Ni-felt AEM electrolyzer in 6 M KOH + seawater. Reproduced with permission from Ref. [69]. Copyright 2023, Wiley-VCH.

4.2.2. Oxyhydroxide Deposition

Compared to the *in situ* fabrication of a polyanion layer, oxyhydroxide deposition during catalyst synthesis is considered a more direct approach to creating an interface. Wu and co-workers reported a CoP_x@FeOOH core-shell nanowire mesh structure for seawater oxidation (Figures 7a to c).[45] The OER overpotentials of CoP_x@FeOOH were measured as 235 and 283 mV to reach 10 and 100 mA cm^{-2} in 1 M KOH seawater, respectively (Figure 7d). The Zeta potential of CoP_x@FeOOH was found to be −18.7 mV, which was lower than that of pristine FeOOH (−14.3 mV). This lower zeta potential suggested an enhanced ability to repel Cl^- ions and improved resistance to chloride corrosion. The HER activity of CoP_x@FeOOH was evaluated in 1 M KOH seawater and was found to be slightly inferior to Co_xP. The decreased HER performance of

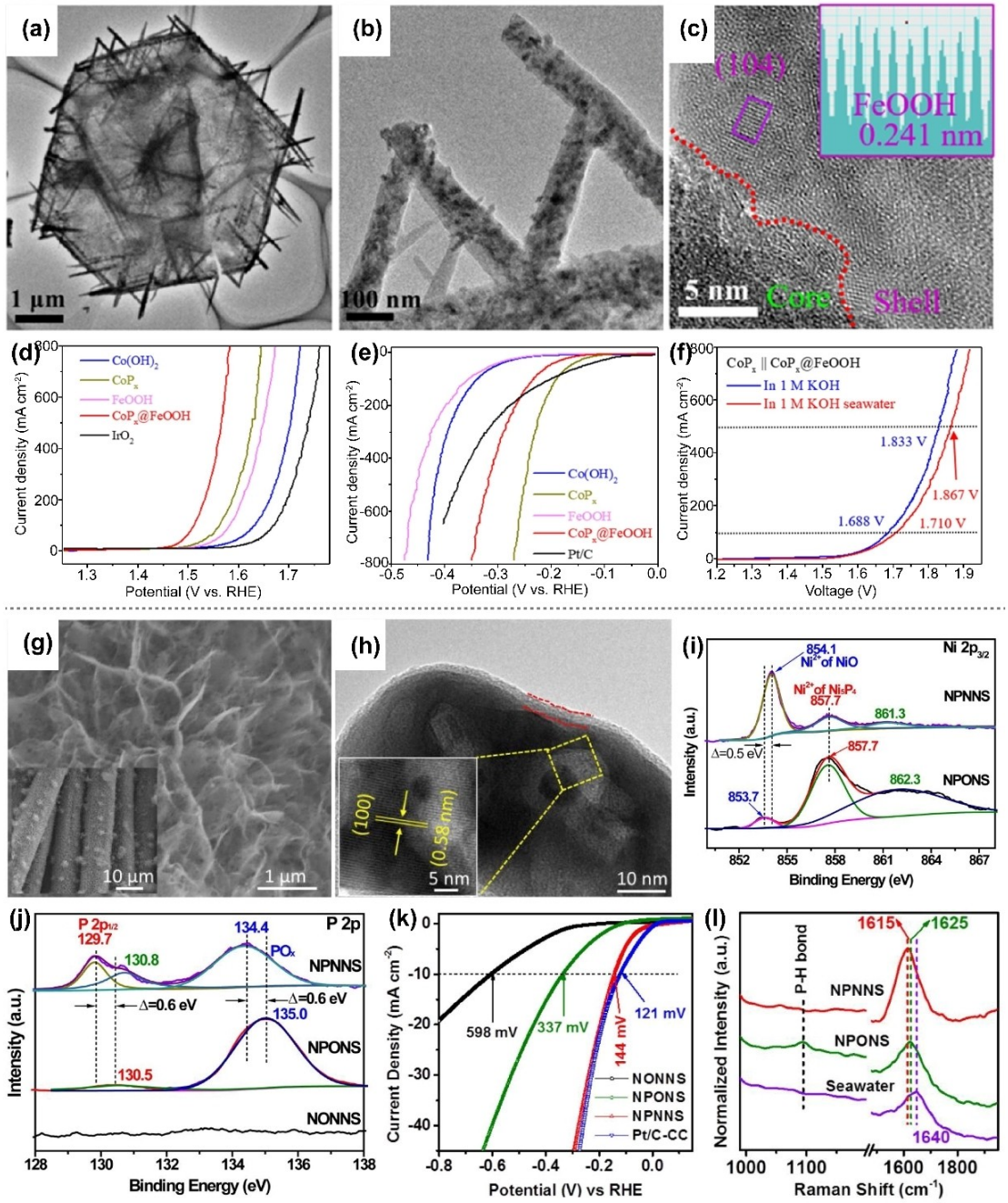

Figure 7. (a–c) TEM images of CoP_x@FeOOH. (d) Anodic and (e) cathodic polarization curves of $Co(OH)_2$, CoP_x, FeOOH, and CoP_x@FeOOH. (f) Polarization curves of $CoP_x||CoP_x$@FeOOH in 1 M KOH and 1 M KOH + seawater. Reproduced with permission from Ref. [45]. Copyright 2021, Elsevier. (g) SEM and (h) TEM images of NPNNS. (i) Ni $2p_{3/2}$ spectra of NPNNS and NPONS. (j) P 2*p* spectra of NPNNS, NPONS, and NONNS. (k) Cathodic polarization curves of NPNNS, NPONS, NONNS, and Pt/C. (l) Raman spectra of NPNNS, NPONS, and seawater. Reproduced with permission from Ref. [70]. Copyright 2019, Elsevier.

CoP_x@FeOOH was attributed to the deposition of the FeOOH layer, which reduced the number of exposed P active sites for trapping H* intermediates and blocked H_2 desorption (Figure 7e). When the $CoP_x||CoP_x$@FeOOH system was employed for overall seawater splitting, 1.549 and 1.710 V were observed to reach 10 and 100 mA cm^{-2}, respectively (Figure 7f).

Huang *et al.* synthesized Ni_5P_4@$Ni_{2+\delta}O_\delta(OH)_{2-\delta}$ by treating the precursor in Ar and N_2 atmospheres, denoted as NPONS and NPNNS, respectively.[70] Additionally, $Ni(OH)_2$ was directly treated under an N_2 atmosphere without a P source (NONNS). SEM and TEM images in Figures 7g and h confirmed the nanosheet morphology and core-shell structure of NPNNS. XPS results in Figures 7i and j revealed a higher intensity of Ni^{2+} of Ni_5P_4 and a lower Ni^{2+} of NiO in NPNNS than in NPONS. This indicated that the ratio of $Ni_{2+\delta}O_\delta(OH)_{2-\delta}$ to Ni_5P_4 in NPONS was lower than that in NPNNS. The negative shift in the P 2*p* binding energies in NPNNS, compared with NPONS, further demonstrated the strong electronic interaction between Ni_{2+}

$_{\delta}O_{\delta}(OH)_{2-\delta}$ and Ni_5P_4 phases. Figure 7k shows that the HER overpotential of NPNNS was 144 mV at 10 mA cm^{-2} in neutral seawater, which was close to commercial Pt/C (121 mV) and significantly better than NPONS (337 mV). Raman spectroscopic analyses in Figure 7l indicated that although the P−H_{ad} bonds were suppressed after the modification of NiOOH on Ni_5P_4, the ability to adsorb H_2O was substantially improved. Furthermore, the negative shift in the O–H vibration peak of NPNNS compared to NPONS suggested weaker O–H bonds of the adsorbed water on NPNNS, thereby enhancing the HER activity.

4.2.3. Modification with Anions

Sun and colleagues designed a phosphate-decorated Ni_3Fe-LDHs@CoP_x catalyst (pd-Ni_3Fe-LDHs@CoP_x) that exhibited a low OER overpotential of 370 mV at 10 mA cm^{-2} in neutral seawater and demonstrated high stability.[71] The modification of phosphate anions onto as-prepared Ni_3Fe-LDHs@CoP_x was achieved by applying a constant voltage of 1.65 V in 1 M PBS (pH = 8) for 12 h. To understand the underlying mechanism, DFT calculations were employed based on the proposed pathway of OER and COR on the surface of Ni_3Fe-LDHs-PO_4^{3-} (Figure 8a). The theoretical OER overpotential for pd-Ni_3Fe-LDHs was calculated to be 0.488 eV (Figure 8b), which is lower than that of Ni_3Fe-LDHs (0.685 eV). This indicated the crucial role of

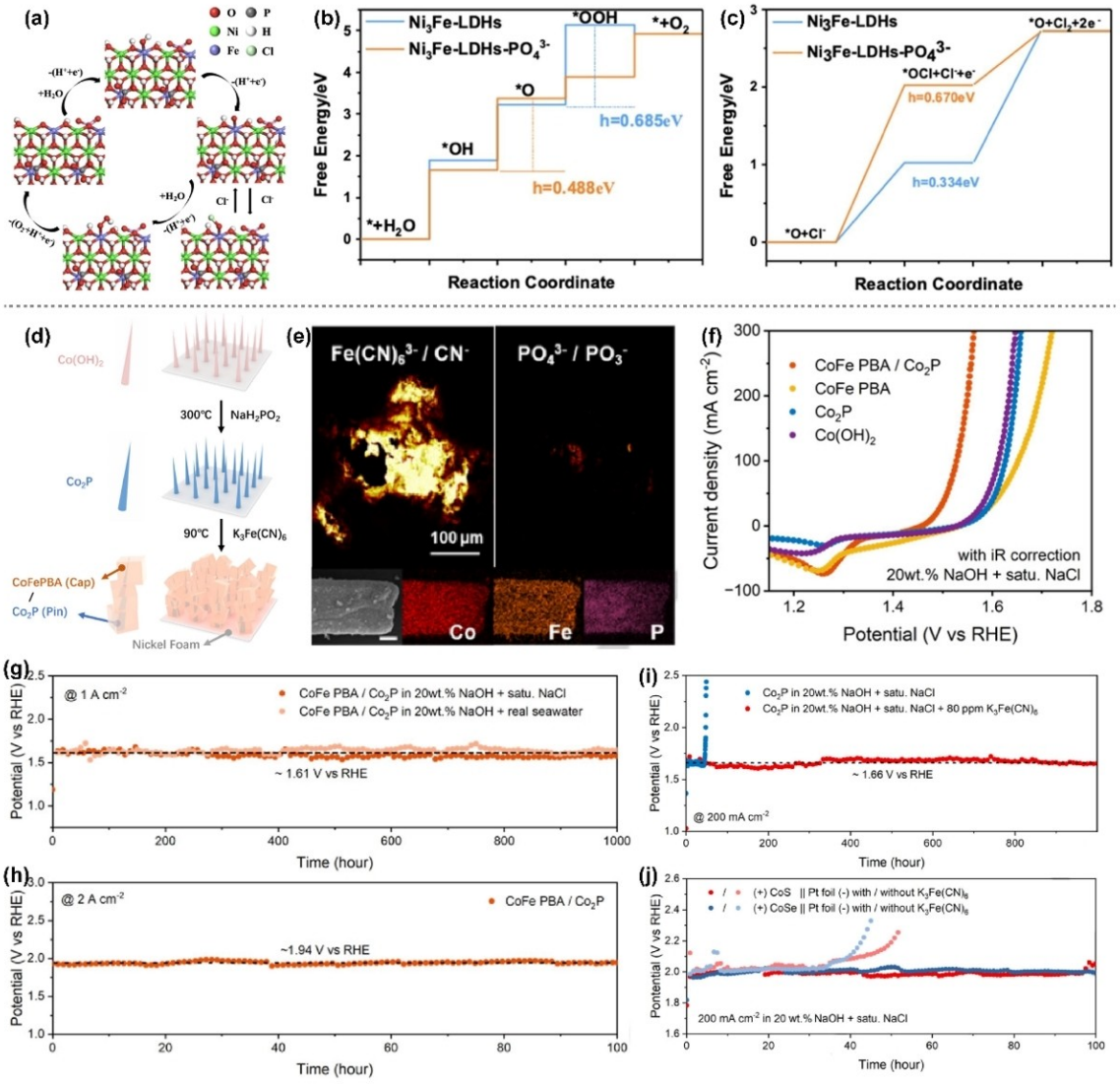

Figure 8. (a) OER and COR mechanisms of Ni_3Fe–LDHs–PO_4^{3-}. Gibbs free energy diagrams of (b) OER and (c) COR on Ni_3Fe–LDHs and Ni_3Fe–LDHs- PO_4^{3-}. Reproduced with permission from Ref. [71]. Copyright 2023, Elsevier. (d) Synthetic route of CoFePBA/Co_2P. (e) TOF-SIMS mappings of $Fe(CN)_6^{3-}$/CN^- and PO_4^{3-}/PO_3^-, and EDX mapping of Co, Fe, and P elements. (f) Anodic polarization curves of CoFePBA/Co_2P, CoFePBA, Co_2P, and $Co(OH)_2$ in 20 wt.% NaOH + saturated NaCl. Chronopotentiometric curves of CoFePBA/Co_2P (g) at 1 A cm^{-2} in 20 wt.% NaOH + saturated NaCl and 20 wt.% NaOH + seawater and (h) at 2 A cm^{-2} in 20 wt.% NaOH + saturated NaCl. Chronopotentiometric curves of (i) Co_2P and (j) CoS||Pt foil and CoSe||Pt foil at 200 mA cm^{-2} in 20 wt.% NaOH + saturated NaCl with and without adding 80 ppm $K_3Fe(CN)_6$. Reproduced with permission from ref. [72]. Copyright 2023, Wiley-VCH.

modified phosphate anions in enhancing the OER performance. The DFT studies supported the conclusion that phosphate anions can decrease the adsorption energy of OH and, consequently, improve the OER performance. Meanwhile, the theoretical COR overpotential of pd-Ni_3Fe-LDHs was calculated as 0.670 eV (Figure 8c), revealing better selectivity for OER over COR.

Liu *et al.* pointed out the beneficial synergistic effect between anions with small radii (*e.g.*, PO_4^{3-} and SO_4^{2-}) and anions with large radii (*e.g.*, $Fe(CN)_6^{3-}$) in improving the stability of TMPs for seawater oxidation.[72] To illustrate this, they employed a secondary hydrothermal treatment to prepare $K_2CoFe(CN)_6/Co_2P$ (CoFePBA/Co_2P, Figure 8d). The coverage of $Fe(CN)_6^{3-}/PO_4^{3-}$ species was confirmed through time of flight secondary ion mass spectrometry (TOF-SIMS) and energy-dispersive X-ray spectroscopy (EDX) elemental mapping (Figure 8e). The as-synthesized CoFePBA/Co_2P exhibited exceptional OER activity, with an overpotential of only 257 mV required to achieve 10 mA cm^{-2} in a solution of 1 M NaOH saturated with NaCl (Figure 8f). Moreover, the potential remained nearly unchanged at high current densities (1 and 2 A cm^{-2}) for 1,000 hours (Figures 8g and h). The significant factor contributing to this excellent OER stability was the synergistic effect between the $Fe(CN)_6^{3-}/PO_4^{3-}$ pair. Pristine Co2P, CoS, and CoSe were used as anodes for seawater oxidation to validate this hypothesis. Due to surface reconstruction during the OER process, small-radius ions (PO_4^{3-}, SO_4^{2-}, and SeO_4^{2-}) were formed on the catalyst surface. However, as depicted in Figures 8i and j, the applied potential only remained stable for a few dozen hours to achieve a current density of 200 mA cm^{-2} in a 20 wt.% NaOH solution saturated with NaCl, after which it increased substantially. Interestingly, when 80 ppm of $K_3Fe(CN)_6$ was added to the electrolyte, these anodes exhibited excellent OER stability, maintaining a stable applied potential even after long-term operation for 100 hours. The primary reason for this improvement is that the *in situ* generated PO_4^{3-}, SO_4^{2-}, and SeO_4^{2-} ions effectively combined with $Fe(CN)_6^{3-}$ species to repel Cl^- ions, thus mitigating the adverse effects of chloride ions on the OER stability.

4.2.4. Carbon Layer Coverage

Carbon materials are generally not recommended as components of electrocatalysts for the OER due to their equilibrium potential for carbon oxidation being 0.207 V (*vs.* SHE).[73] However, this drawback can be advantageous in seawater splitting. When carbon materials undergo partial oxidation on their surface, they generate OH^-/CO_3^{2-} ions that effectively repel Cl^- ions in seawater. Moreover, carbon coating assists to enhance electronic conductivity and modify the electronic states of catalysts, thereby promoting the OER activity.

Wang and colleagues synthesized Co_xP nanowire arrays with P vacancies encapsulated in N-doped carbon layers (Co_xP_v@NC) that exhibited an overpotential of 386 mV to reach 1 A cm^{-2} in 1 M KOH seawater.[46] Remarkably, after maintaining a current density of 0.8 A cm^{-2} for 100 h, the overpotential of Co_xP_v@NC only slightly changed, indicating its excellent stability. Additionally, the synergistic effect between Co_xP_v and NC improved the HER activity of Co_xP_v@NC, with an overpotential of 232 mV at 1 A cm^{-2}, surpassing that of Co_xP_v (250 mV). The assembled Co_xP_v@NC||Co_xP_v@NC electrolyzer exhibited a cell voltage of 1.88 V to provide 1 A cm^{-2} in 1 M KOH seawater. Zheng *et al.* prepared FeCoP nanoparticles on reduced graphene oxide-coated Ni foam (FeCoP@rGO/NF) for seawater oxidation.[74] The introduction of the rGO layer facilitated electron transfer from Fe (Co) atoms to P atoms, leading to electronic redistribution. FeCoP@rGO/NF demonstrated enhanced OER activity with an overpotential of 257 mV at 200 mA cm^{-2} in 1 M KOH solution compared to FeCoP/NF. Moreover, the OER activities of FeCoP@rGO/NF in alkaline simulated seawater (1 M KOH + 0.5 M NaCl) and alkaline natural seawater (1 M KOH + seawater) closely resembled that in 1 M KOH, with overpotentials of 282 and 281 mV, respectively. The stability of FeCoP@rGO/NF was evaluated at 50 mA cm^{-2} for 200 h in 1 M KOH + seawater, and no loss of current density was observed, demonstrating its excellent and stable OER performance. Wang's group modified an ultrathin carbon layer on a CoP–FeP heterostructure for overall seawater splitting.[47] The intense interaction between the carbon layer and CoP–FeP resulted in higher OER and HER activities for C@CoP–FeP compared to CoP–FeP in 1 M KOH + 0.5 M NaCl. The cell voltage of the C@CoP–FeP||C@CoP–FeP electrolyzer was only 1.73 V to achieve 100 mA cm^{-2} in simulated seawater splitting.

4.2.5. 3D Hierarchical Structure

The deposition of hydroxides, such as $Mg(OH)_2$ and $Ca(OH)_2$, with poor activity and low conductivity, pose another significant challenge in direct seawater splitting. Constructing a 3D hierarchical structure is a promising strategy to minimize this impact. By utilizing a 3D nanostructure as a substrate to support nanosized TMPs, a larger specific surface area can be achieved compared to conventional catalysts. This increased surface area allows for more active sites for catalytic reactions, thereby prolonging the deactivation duration caused by hydroxide deposition on the electrode. The 3D substrate, when it is covered with TMPs, also helps to maintain the original state of TMPs and provides stable channels for electron transfer.

In the study conducted by Chang *et al.*, they designed a 3D hierarchical structure consisting of heterogeneous Ni_2P–$NiSe_2$ nanosheets grown on ZnP nanorod arrays (ZnP@Ni_2P–$NiSe_2$, Figure 9a).[75] The core-shell structure of ZnP@Ni_2P–$NiSe_2$ was characterized using TEM images (Figures 9b and c). The vertical nanorod arrays on Ni foam provided a high specific surface area of 14.7 m^2 g^{-1} for ZnP@Ni_2P–$NiSe_2$, which was significantly higher than that of pure ZnP nanorods and other traditional catalysts, such as CoP nanoparticles,[76] MoP/C composite,[77] β-$Ni(OH)_2$/NF.[78] The crystal structure of Ni_2P–$NiSe_2$ was established (Figure 9d), and four sites were proposed as the real active sites for the HER: 1) Ni in the Ni_2P phase, 2) Ni in the Ni_2P phase, 3) Ni in the $NiSe_2$ phase, and 4) Se in the $NiSe_2$ phase. DFT calculations showed that the energy barrier on Ni in the

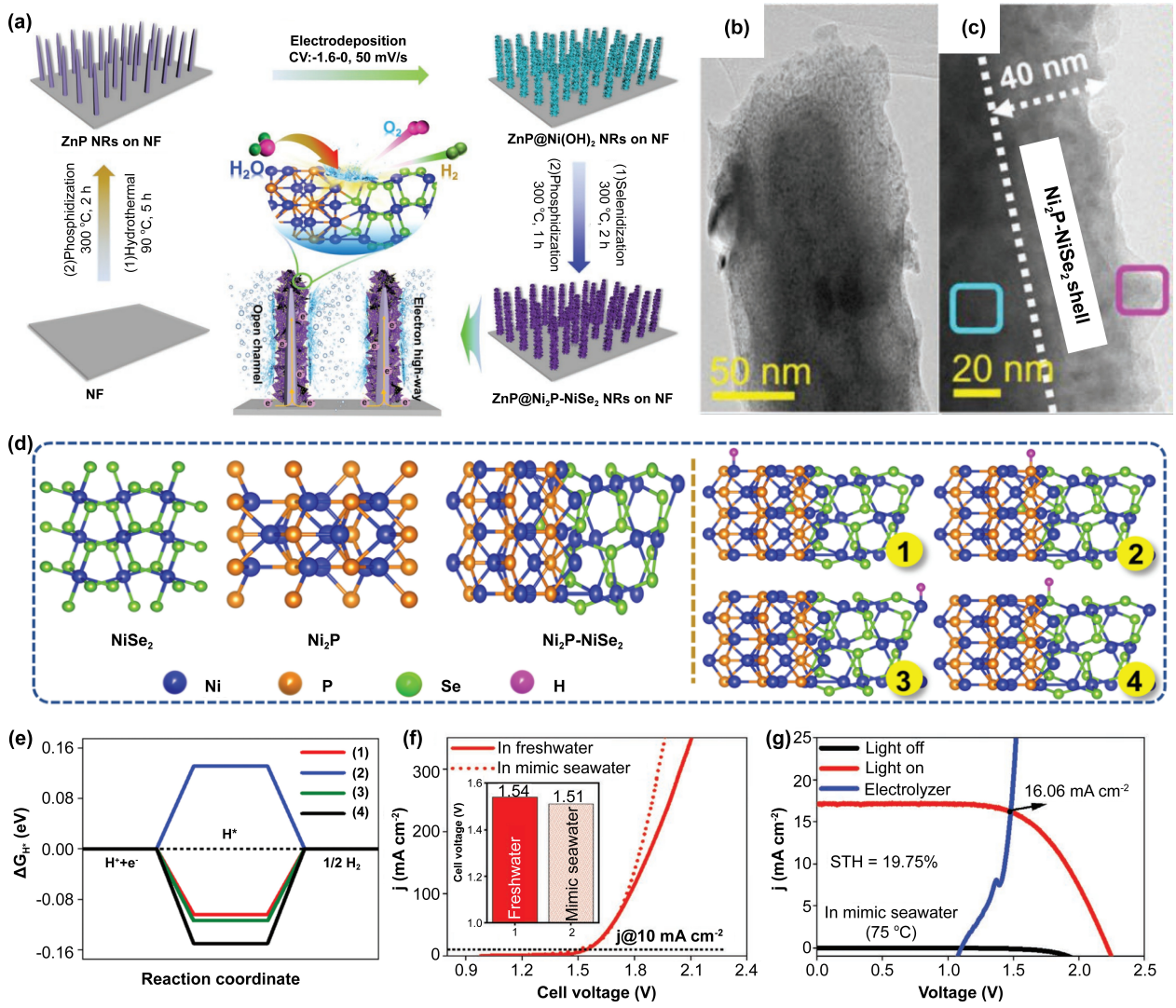

Figure 9. (a) Illustration of the synthetic route of ZnP@Ni_2P–$NiSe_2$ on Ni foam. (b and c) TEM images of ZnP@Ni_2P–$NiSe_2$. (d) Crystal structures of Ni_2P, $NiSe_2$, and Ni_2P–$NiSe_2$, and four proposed active sites for HER. (e) Gibbs free energies of hydrogen generation on the four active sites. (f) Polarization curves of ZnP@Ni_2P–$NiSe_2$ in freshwater and simulated seawater. (g) J–V curves of the commercial solar cell and polarization curve of ZnP@Ni_2P–$NiSe_2$ device for seawater splitting at 75 °C. Reproduced with permission from Ref. [75]. Copyright 2022, Wiley-VCH.

Ni_2P phase was the lowest, indicating its responsibility for the HER (Figure 9e). The OER and HER activities of ZnP@Ni_2P–$NiSe_2$ were evaluated in 1 M KOH, and the overpotentials were 326 and 214 mV at 100 mA cm^{-2}, respectively, which were smaller than those of ZnP@$Ni(OH)_2$, ZnP@$NiSe_2$, and ZnP@Ni_2P. Interestingly, the ZnP@Ni_2P–$NiSe_2$||ZnP@Ni_2P–$NiSe_2$ electrolyzer required a voltage of 1.51 V to obtain 10 mA cm^{-2} at 25 °C in alkaline simulated seawater (Figure 9f), which is lower than that in alkaline freshwater (1.54 V). The reduced voltage indicated that the presence of salt in the electrolyte did not diminish the catalytic performance of seawater splitting. The conductivity of the electrolyte was improved due to the presence of salt, resulting in enhanced catalytic performance. Furthermore, a commercial solar cell was employed to power the double ZnP@Ni_2P–$NiSe_2$ electrolyzer (Figure 9g), demonstrating a high solar-to-hydrogen efficiency of 19.75 %.

5. Conclusion and Future Perspectives

The concept of direct seawater electrolysis for hydrogen production is theoretically attractive but practically challenging, largely due to the myriad of impurities found in natural seawater. These impurities introduce complications such as competitive COR, accelerated corrosion of system components, and detrimental poisoning effects on the catalytic materials. Therefore, developing electrocatalysts through sophisticated design principles is critical for overcoming these barriers, thus enabling efficient and robust seawater electrolysis characterized by enhanced activity, selectivity, and stability. In this context, TMPs have emerged as a focus of research interest, owing to their promising electrocatalytic performance in seawater splitting applications. Various innovative strategies have been pursued to augment the intrinsic activity of TMPs and to minimize the occurrence of side reactions in the saline medium.

Although these electrocatalysts have exhibited exemplary performance in alkaline-seawater mixtures (1 M KOH + seawater), their effectiveness is significantly compromised in neutral seawater conditions (pH ~8) due to the diminished concentrations of H^+ and OH^- ions, which are instrumental for the kinetics of the OER and HER.

While there have been considerable advancements in the design of highly active TMPs, the catalysts available today have not yet reached the performance benchmarks necessary for hydrogen production on an industrial scale, particularly in the areas of catalytic activity and stability. Therefore, practical applications require further advancements. Here are some perspectives for future research in this field:

1) Improving the intrinsic activity
   Despite the outstanding activities demonstrated by recently reported TMPs in alkaline seawater, their application in untreated natural seawater remains a formidable challenge. To address this, it is imperative to optimize the adsorption energies of reaction intermediates and facilitate the dissociation of H_2O on the active sites of TMPs. Among the transition metals, Fe, Co, Ni, and Mn are generally recognized as the primary active species for seawater splitting. Modifying the electronic states through the adjustment of coordination environments, such as the introduction of different elements, is a crucial avenue for enhancement. Additionally, the synthesis of bi-metallic active sites proves to be an effective strategy in augmenting electrocatalytic activity. The synergistic effects arising from the interaction between multiple elements can contribute to a substantial improvement in catalytic performance.
2) Increasing the number of active sites
   Increasing the number of active sites in TMPs represents an effective strategy to enhance catalytic activity. Abundant active sites not only improve utilization but also mitigate catalyst decay caused by the deposition of impurity ions in seawater. Strategies such as designing TMPs with a porous structure or an ultrathin 2D layer can be employed to achieve this goal. Moreover, coupling TMPs with diverse substrates, including nitrides, sulfides, selenides, and carbides, carries remarkable potential in adjusting the electronic state of active sites and thereby enhancing seawater splitting activity. The exploration of these alternative materials opens new avenues for gaining insights and opportunities to improve catalytic performance.
3) Advancing mechanism research
   Despite the challenges posed by the intricate environment of natural seawater, the estimation and theoretical comprehension of electrocatalyst behavior are essential for modifying catalysts with both high activity and long-term stability. Achieving a better understanding of electrocatalyst performance in seawater necessitates the incorporation of computational methods, such as DFT calculations, and the application of *in situ* characterization techniques. *In situ* Raman spectroscopy, synchrotron radiation spectroscopy, and Fourier transform infrared spectroscopy are invaluable tools for providing real-time insights into structural transformations and reaction pathways, enabling a more comprehensive understanding of electrocatalytic processes in seawater and the identification of fundamental issues that limit catalytic activity. Such knowledge serves as a guide in designing highly active catalysts tailored for efficient seawater splitting.

Acknowledgements

This work was financially supported by Anhui Polytechnic University research start-up fund (No.2022YQQ045) and the Hong Kong Polytechnic University (1-ZVST and Q-CDAG).

Conflict of Interests

The authors declare no conflict of interest.

Keywords: transition metal phosphides · seawater splitting · structural modification · interface engineering

[1] P. E. Brockway, A. Owen, L. I. Brand-Correa, L. Hardt, *Nat. Energy* **2019**, *4*, 612–621.
[2] M. Yue, H. Lambert, E. Pahon, R. Roche, S. Jemei, D. Hissel, *Renewable Sustainable Energy Rev.* **2021**, *146*, 111180.
[3] Y. Li, X. Wei, L. Chen, J. Shi, M. He, *Nat. Commun.* **2019**, *10*, 5335.
[4] J. N. Hausmann, R. Schlögl, P. W. Menezes, M. Driess, *Energy Environ. Sci.* **2021**, *14*, 3679–3685.
[5] J. Liu, S. Duan, H. Shi, T. Wang, X. Yang, Y. Huang, G. Wu, Q. Li, *Angew. Chem. Int. Ed.* **2022**, *61*, e202210753.
[6] A. Bradshaw, K. Schleicher, *IEEE J. Oceanic Eng.* **1980**, *5*, 50–62.
[7] K. Sood, S. Rana, R. Wadhwa, K. K. Bhasin, M. Jha, *Adv. Mater. Interfaces* **2022**, *9*, 2201138.
[8] a) J. Wang, D. F. Thomas, A. Chen, *Anal. Chem.* **2008**, *80*, 997–1004; b) S. Park, T. D. Chung, H. C. Kim, *Anal. Chem.* **2003**, *75*, 3046–3049.
[9] a) J. Zeng, L. Zhang, Q. Zhou, L. Liao, Y. Qi, H. Zhou, D. Li, F. Cai, H. Wang, D. Tang, F. Yu, *Small* **2022**, *18*, 2104624; b) B. Zhang, Y. Zheng, T. Ma, C. Yang, Y. Peng, Z. Zhou, M. Zhou, S. Li, Y. Wang, C. Cheng, *Adv. Mater.* **2021**, *33*, 2006042.
[10] a) P. M. Bodhankar, P. B. Sarawade, G. Singh, A. Vinu, D. S. Dhawale, *J. Mater. Chem. A* **2021**, *9*, 3180–3208; b) S. Anantharaj, S. Kundu, S. Noda, *J. Mater. Chem. A* **2020**, *8*, 4174–4192; c) S. Dutta, A. Indra, Y. Feng, H. Han, T. Song, *Appl. Catal. B* **2019**, *241*, 521–527; d) F.-C. Shen, S.-N. Sun, Z.-F. Xin, S.-L. Li, L.-Z. Dong, Q. Huang, Y.-R. Wang, J. Liu, Y.-Q. Lan, *Appl. Catal. B* **2019**, *243*, 470–480; e) Z. Kou, L. Zhang, Y. Ma, X. Liu, W. Zang, J. Zhang, S. Huang, Y. Du, A. K. Cheetham, J. Wang, *Appl. Catal. B* **2019**, *243*, 678–685; f) M. Wang, L. Zhang, Y. He, H. Zhu, *J. Mater. Chem. A* **2021**, *9*, 5320–5363.
[11] a) F. Yu, H. Zhou, Y. Huang, J. Sun, F. Qin, J. Bao, W. A. Goddard, S. Chen, Z. Ren, *Nat. Commun.* **2018**, *9*, 2551; b) X. Wang, W. Li, D. Xiong, D. Y. Petrovykh, L. Liu, *Adv. Funct. Mater.* **2016**, *26*, 4067–4077; c) J. Yu, Q. Li, Y. Li, C.-Y. Xu, L. Zhen, V. P. Dravid, J. Wu, *Adv. Funct. Mater.* **2016**, *26*, 7644–7651.
[12] E. J. Popczun, J. R. McKone, C. G. Read, A. J. Biacchi, A. M. Wiltrout, N. S. Lewis, R. E. Schaak, *J. Am. Chem. Soc.* **2013**, *135*, 9267–9270.
[13] K. Ojha, S. Saha, P. Dagar, A. K. Ganguli, *Phys. Chem. Chem. Phys.* **2018**, *20*, 6777–6799.
[14] a) H. Chu, P. Feng, B. Jin, G. Ye, S. Cui, M. Zheng, G.-X. Zhang, M. Yang, *Chem. Eng. J.* **2022**, *433*, 133523; b) W. Zou, C. Sun, K. Zhao, J. Li, X. Pan, D. Ye, Y. Xie, W. Xu, H. Zhao, L. Zhang, J. Zhang, *Electrochim. Acta* **2020**, *345*, 136114.
[15] a) L. Yu, L. Wu, S. Song, B. McElhenny, F. Zhang, S. Chen, Z. Ren, *ACS Energy Lett.* **2020**, *5*, 2681–2689; b) J. Wang, Y. Zhang, W. Zhang, Q. Zhao, J. Li, G. Liu, *Electrochim. Acta* **2023**, *438*, 141563; c) Y. Cong, X. Chen, Y. Mei, J. Ye, T.-T. Li, *Dalton Trans.* **2022**, *51*, 2923–2931.
[16] A. Ray, S. Sultana, L. Paramanik, K. M. Parida, *J. Mater. Chem. A* **2020**, *8*, 19196–19245.

[17] M. Chatenet, B. G. Pollet, D. R. Dekel, F. Dionigi, J. Deseure, P. Millet, R. D. Braatz, M. Z. Bazant, M. Eikerling, I. Staffell, P. Balcombe, Y. Shao-Horn, H. Schäfer, *Chem. Soc. Rev.* **2022**, *51*, 4583–4762.
[18] F. Dionigi, T. Reier, Z. Pawolek, M. Gliech, P. Strasser, *ChemSusChem* **2016**, *9*, 962–972.
[19] a) H. You, D. Wu, D. Si, M. Cao, F. Sun, H. Zhang, H. Wang, T.-F. Liu, R. Cao, *J. Am. Chem. Soc.* **2022**, *144*, 9254–9263; b) L. Yu, Q. Zhu, S. Song, B. McElhenny, D. Wang, C. Wu, Z. Qin, J. Bao, Y. Yu, S. Chen, Z. Ren, *Nat. Commun.* **2019**, *10*, 5106; c) X. H. Wang, Y. Ling, B. Wu, B. L. Li, X. L. Li, J. L. Lei, N. B. Li, H. Q. Luo, *Nano Energy* **2021**, *87*, 106160.
[20] a) D. W. Kirk, A. E. Ledas, *Int. J. Hydrogen Energy* **1982**, *7*, 925–932; b) W. Tong, M. Forster, F. Dionigi, S. Dresp, R. Sadeghi Erami, P. Strasser, A. J. Cowan, P. Farràs, *Nat. Energy* **2020**, *5*, 367–377.
[21] Y. Han, Y. Chen, R. Fan, Z. Li, Z. Zou, *EcoMat* **2021**, *3*, e12097.
[22] K. Xu, H. Ding, M. Zhang, M. Chen, Z. Hao, L. Zhang, C. Wu, Y. Xie, *Adv. Mater.* **2017**, *29*, 1606980.
[23] H.-W. Man, C.-S. Tsang, M. M.-J. Li, J. Mo, B. Huang, L. Y. S. Lee, Y.-C. Leung, K.-Y. Wong, S. C. E. Tsang, *Chem. Commun.* **2018**, *54*, 8630–8633.
[24] H. Wan, L. Li, Y. Chen, J. Gong, M. Duan, C. Liu, J. Zhang, H. Wang, *Electrochim. Acta* **2017**, *229*, 380–386.
[25] Y. Lin, K. Sun, S. Liu, X. Chen, Y. Cheng, W.-C. Cheong, Z. Chen, L. Zheng, J. Zhang, X. Li, Y. Pan, C. Chen, *Adv. Energy Mater.* **2019**, *9*, 1901213.
[26] P. He, X.-Y. Yu, X. W. Lou, *Angew. Chem. Int. Ed.* **2017**, *56*, 3897–3900.
[27] M. Ledendecker, S. Krick Calderón, C. Papp, H.-P. Steinrück, M. Antonietti, M. Shalom, *Angew. Chem. Int. Ed.* **2015**, *54*, 12361–12365.
[28] a) H. Zhao, S. Sun, P. Jiang, Z. J. Xu, *Chem. Eng. J.* **2017**, *315*, 296–303; b) X. Zhang, A. Wu, X. Wang, C. Tian, R. An, H. Fu, *J. Mater. Chem. A* **2018**, *6*, 17905–17914.
[29] H. Liang, C. Xia, Q. Jiang, A. N. Gandi, U. Schwingenschlögl, H. N. Alshareef, *Nano Energy* **2017**, *35*, 331–340.
[30] a) V. T. Chebrolu, B. Balakrishnan, S. A. Raja, I. Cho, J.-S. Bak, H.-J. Kim, *New J. Chem.* **2020**, *44*, 7690–7697; b) W. Li, M. Chen, Y. Lu, P. Qi, G. Liu, Y. Zhao, H. Wu, Y. Tang, *Appl. Surf. Sci.* **2022**, *598*, 153717.
[31] a) L. Chai, S. Liu, S. Pei, C. Wang, *Chem. Eng. J.* **2021**, *420*, 129686; b) C. Wang, Y. Wu, Z. Zhou, J. Wang, S. Pei, S. Liu, *Int. J. Hydrogen Energy* **2022**, *47*, 40849–40859.
[32] M.-I. Jamesh, M. Harb, *J. Energy Chem.* **2021**, *56*, 299–342.
[33] S. Wang, P. Yang, X. Sun, H. Xing, J. Hu, P. Chen, Z. Cui, W. Zhu, Z. Ma, *Appl. Catal. B* **2021**, *297*, 120386.
[34] Y. Yu, J. Li, J. Luo, Z. Kang, C. Jia, Z. Liu, W. Huang, Q. Chen, P. Deng, Y. Shen, X. Tian, *Mater. Today Nano* **2022**, *18*, 100216.
[35] Y. Song, M. Sun, S. Zhang, X. Zhang, P. Yi, J. Liu, B. Huang, M. Huang, L. Zhang, *Adv. Funct. Mater.* **2023**, *33*, 2214081.
[36] S. Loomba, M. W. Khan, M. Haris, S. M. Mousavi, A. Zavabeti, K. Xu, A. Tadich, L. Thomsen, C. F. McConville, Y. Li, S. Walia, N. Mahmood, *Small* **2023**, *19*, 2207310.
[37] T. Zhao, S. Wang, C. Jia, C. Rong, Z. Su, K. Dastafkan, Q. Zhang, C. Zhao, *Small* **2023**, *19*, 2208076.
[38] Y. Wang, B. Li, W. Xiao, X. Wang, Y. Fu, Z. Li, G. Xu, J. Lai, Z. Wu, L. Wang, *Chem. Eng. J.* **2023**, *452*, 139175.
[39] L. Wu, L. Yu, F. Zhang, B. McElhenny, D. Luo, A. Karim, S. Chen, Z. Ren, *Adv. Funct. Mater.* **2021**, *31*, 2006484.
[40] J. Li, M. Song, Y. Hu, C. Zhang, W. Liu, X. Huang, J. Zhang, Y. Zhu, J. Zhang, D. Wang, *Nano Res.* **2023**, *16*, 3658–3664.
[41] H.-Y. Wang, J.-T. Ren, L. Wang, M.-L. Sun, H.-M. Yang, X.-W. Lv, Z.-Y. Yuan, *J. Energy Chem.* **2022**, *75*, 66–73.
[42] Y. Luo, P. Wang, G. Zhang, S. Wu, Z. Chen, H. Ranganathan, S. Sun, Z. Shi, *Chem. Eng. J.* **2023**, *454*, 140061.
[43] Q. Ma, H. Jin, F. Xia, H. Xu, J. Zhu, R. Qin, H. Bai, B. Shuai, W. Huang, D. Chen, Z. Li, J. Wu, J. Yu, S. Mu, *J. Mater. Chem. A* **2021**, *9*, 26852–26860.
[44] S. Lv, Y. Deng, Q. Liu, Z. Fu, X. Liu, M. Wang, Z. Xiao, B. Li, L. Wang, *Appl. Catal. B* **2023**, *326*, 122403.
[45] L. Wu, L. Yu, B. McElhenny, X. Xing, D. Luo, F. Zhang, J. Bao, S. Chen, Z. Ren, *Appl. Catal. B* **2021**, *294*, 120256.
[46] X. Wang, X. Liu, S. Wu, K. Liu, X. Meng, B. Li, J. Lai, L. Wang, S. Feng, *Nano Energy* **2023**, *109*, 108292.
[47] J. Li, Y. Hu, X. Huang, Y. Zhu, D. Wang, *Small* **2023**, *19*, 2206533.
[48] P. Yang, Z. Zhang, C. Jin, M. Ren, J. Wang, T. Shi, H. Xing, X. Ji, *Langmuir* **2023**, *39*, 6240–6248.
[49] H. K. Sadhanala, A. Gupta, A. Gedanken, *Sustain. Energy Fuels* **2023**, *7*, 4677–4686.
[50] C. Fu, W. Hao, J. Fan, Q. Zhang, Y. Guo, J. Fan, Z. Chen, G. Li, *Small* **2023**, *19*, 2205689.
[51] F. Zhang, Y. Liu, F. Yu, H. Pang, X. Zhou, D. Li, W. Ma, Q. Zhou, Y. Mo, H. Zhou, *ACS Nano* **2023**, *17*, 1681–1692.
[52] W. Ma, D. Li, L. Liao, H. Zhou, F. Zhang, X. Zhou, Y. Mo, F. Yu, *Small* **2023**, *19*, 2207082.
[53] R.-Q. Li, B.-L. Wang, T. Gao, R. Zhang, C. Xu, X. Jiang, J. Zeng, Y. Bando, P. Hu, Y. Li, X.-B. Wang, *Nano Energy* **2019**, *58*, 870–876.
[54] J. Liu, X. Liu, H. Shi, J. Luo, L. Wang, J. Liang, S. Li, L.-M. Yang, T. Wang, Y. Huang, Q. Li, *Appl. Catal. B* **2022**, *302*, 120862.
[55] Y. Lin, K. Sun, X. Chen, C. Chen, Y. Pan, X. Li, J. Zhang, *J. Energy Chem.* **2021**, *55*, 92–101.
[56] X. Sun, P. Yang, S. Wang, J. Hu, P. Chen, H. Xing, W. Zhu, *Inter. J. Hydrog. Energy* **2022**, *47*, 28495–28504.
[57] W. Xu, G. Fan, S. Zhu, Y. Liang, Z. Cui, Z. Li, H. Jiang, S. Wu, F. Cheng, *Adv. Funct. Mater.* **2021**, *31*, 2107333.
[58] W. Zhang, X. Liu, Q. Yu, X. Wang, H. Mao, J. Chi, B. Li, J. Wan, L. Wang, *Chem. Eng. J.* **2023**, *454*, 140210.
[59] C. Lyu, C. Cao, J. Cheng, Y. Yang, K. Wu, J. Wu, W.-M. Lau, P. Qian, N. Wang, J. Zheng, *Chem. Eng. J.* **2023**, *464*, 142538.
[60] D. Liu, H. Ai, M. Chen, P. Zhou, B. Li, D. Liu, X. Du, K. H. Lo, K.-W. Ng, S.-P. Wang, S. Chen, G. Xing, J. Hu, H. Pan, *Small* **2021**, *17*, 2007557.
[61] R. Boppella, J. Tan, W. Yang, J. Moon, *Adv. Funct. Mater.* **2019**, *29*, 1807976.
[62] Y. Lin, Y. Pan, S. Liu, K. Sun, Y. Cheng, M. Liu, Z. Wang, X. Li, J. Zhang, *Appl. Catal. B* **2019**, *259*, 118039.
[63] H. Liu, X. Ma, H. Hu, Y. Pan, W. Zhao, J. Liu, X. Zhao, J. Wang, Z. Yang, Q. Zhao, H. Ning, M. Wu, *ACS Appl. Mater. Interfaces* **2019**, *11*, 15528–15536.
[64] C. Chai, J. Yang, C. Jiang, L. Liu, J. Xi, *ACS Appl. Energ. Mater.* **2022**, *5*, 2909–2917.
[65] D. Chen, Z. Pu, R. Lu, P. Ji, P. Wang, J. Zhu, C. Lin, H.-W. Li, X. Zhou, Z. Hu, F. Xia, J. Wu, S. Mu, *Adv. Energy Mater.* **2020**, *10*, 2000814.
[66] M. Qu, Y. Jiang, M. Yang, S. Liu, Q. Guo, W. Shen, M. Li, R. He, *Appl. Catal. B* **2020**, *263*, 118324.
[67] D. Wu, B. Liu, R. Li, D. Chen, W. Zeng, H. Zhao, Y. Yao, R. Qin, J. Yu, L. Chen, J. Zhang, B. Li, S. Mu, *Small* **2023**, *19*, 2300030.
[68] Z. Wang, Y. Wang, J. Wang, W. Xiao, G. Xu, Z. Li, C. Dai, H. Zhang, Z. Wu, L. Wang, *Appl. Surf. Sci.* **2023**, *623*, 157026.
[69] C. Huang, Q. Zhou, L. Yu, D. Duan, T. Cao, S. Qiu, Z. Wang, J. Guo, Y. Xie, L. Li, Y. Yu, *Adv. Energy Mater.* **2023**, *13*, 2301475.
[70] Y. Huang, L. Hu, R. Liu, Y. Hu, T. Xiong, W. Qiu, M. S. Balogun, A. Pan, Y. Tong, *Appl. Catal. B* **2019**, *251*, 181–194.
[71] T. Li, X. Zhao, M. Getaye Sendeku, X. Zhang, L. Xu, Z. Wang, S. Wang, X. Duan, H. Liu, W. Liu, D. Zhou, H. Xu, Y. Kuang, X. Sun, *Chem. Eng. J.* **2023**, *460*, 141413.
[72] W. Liu, J. Yu, M. G. Sendeku, T. Li, W. Gao, G. Yang, Y. Kuang, X. Sun, *Angew. Chem. Int. Ed.* **2023**, *62*, e202309882.
[73] B. Avasarala, R. Moore, P. Haldar, *Electrochim. Acta* **2010**, *55*, 4765–4771.
[74] Y. Zheng, D. Yu, W. Xu, K. Zhang, K. Ma, X. Guo, Y. Lou, M. Hu, *Dalton Trans.* **2023**, *52*, 3493–3500.
[75] K. Chang, D. T. Tran, J. Wang, S. Prabhakaran, D. H. Kim, N. H. Kim, J. H. Lee, *Adv. Funct. Mater.* **2022**, *32*, 2113224.
[76] M. Liu, J. Li, *ACS Appl. Mater. Interfaces* **2016**, *8*, 2158–2165.
[77] R. Ge, J. Huo, T. Liao, Y. Liu, M. Zhu, Y. Li, J. Zhang, W. Li, *Appl. Catal. B* **2020**, *260*, 118196.
[78] J.-H. Yang, X. Xu, M. Chen, D. Yang, H. Lu, Y. Sun, C. Shao, Q. Song, J. Zhang, L. Gao, Y. Zhang, *J. Electroanal. Chem.* **2021**, *882*, 115035.

Manuscript received: December 21, 2023
Revised manuscript received: February 21, 2024
Accepted manuscript online: March 13, 2024
Version of record online: April 22, 2024